AD

BRL MR 2

BRL

MEMORANDUM REPORT NO. 2551

TESTS OF AN ELLIPSOIDAL MIRROR
REFLECTOMETER

John D. Sullivan, Jr.
Frank J. Allen

October 1975

Approved for public release; distribution unlimited.

USA BALLISTIC RESEARCH LABORATORIES
ABERDEEN PROVING GROUND, MARYLAND

REPORT DOCUMENTATION PAGE		READ INSTRUCTIONS BEFORE COMPLETING FORM
1. REPORT NUMBER BRL MEMORANDUM REPORT NO. 2551	2. GOVT ACCESSION NO.	3. RECIPIENT'S CATALOG NUMBER
4. TITLE (and Subtitle) TESTS OF AN ELLIPSOIDAL MIRROR REFLECTOMETER		5. TYPE OF REPORT & PERIOD COVERED
		6. PERFORMING ORG. REPORT NUMBER
7. AUTHOR(s) John D. Sullivan, Jr., Frank J. Allen		8. CONTRACT OR GRANT NUMBER(s)
9. PERFORMING ORGANIZATION NAME AND ADDRESS U. S. Army Ballistic Research Laboratories Aberdeen Proving Ground, Maryland 21005		10. PROGRAM ELEMENT, PROJECT, TASK AREA & WORK UNIT NUMBERS
11. CONTROLLING OFFICE NAME AND ADDRESS U. S. Army Materiel Command 5001 Eisenhower Avenue Washington, D. C. 22333		12. REPORT DATE OCTOBER 1975
		13. NUMBER OF PAGES 60
14. MONITORING AGENCY NAME & ADDRESS(If different from Controlling Office)		15. SECURITY CLASS. (of this report) UNCLASSIFIED
		15a. DECLASSIFICATION/DOWNGRADING SCHEDULE

16. DISTRIBUTION STATEMENT (of this Report)

Approved for Public release; distribution unlimited

17. DISTRIBUTION STATEMENT (of the abstract entered in Block 20, if different from Report)

18. SUPPLEMENTARY NOTES

19. KEY WORDS (Continue on reverse side if necessary and identify by block number)

reflectometer
ellipsoidal mirror
reflectance

20. ABSTRACT (Continue on reverse side if necessary and identify by block number) Apparatus was assembled to form a reflectometer based on an ellipsoidal mirror. The target is mounted with provision for flame heating and temperature sensing. Reflectance measurements in the near infrared were compared with those taken with a commercial instrument, a Beckman DK-2A. The result is a 16% disagreement which is attributed to sensitivity to the reflectance pattern from a unidirectionally scratched target. The reflectance data scatter is ±0.04 with the ellipsoidal mirror; the scatter is seven times less with the Beckman. An improved averaging sphere coating will be necessary for making reflectance measurements in the middle infrared.
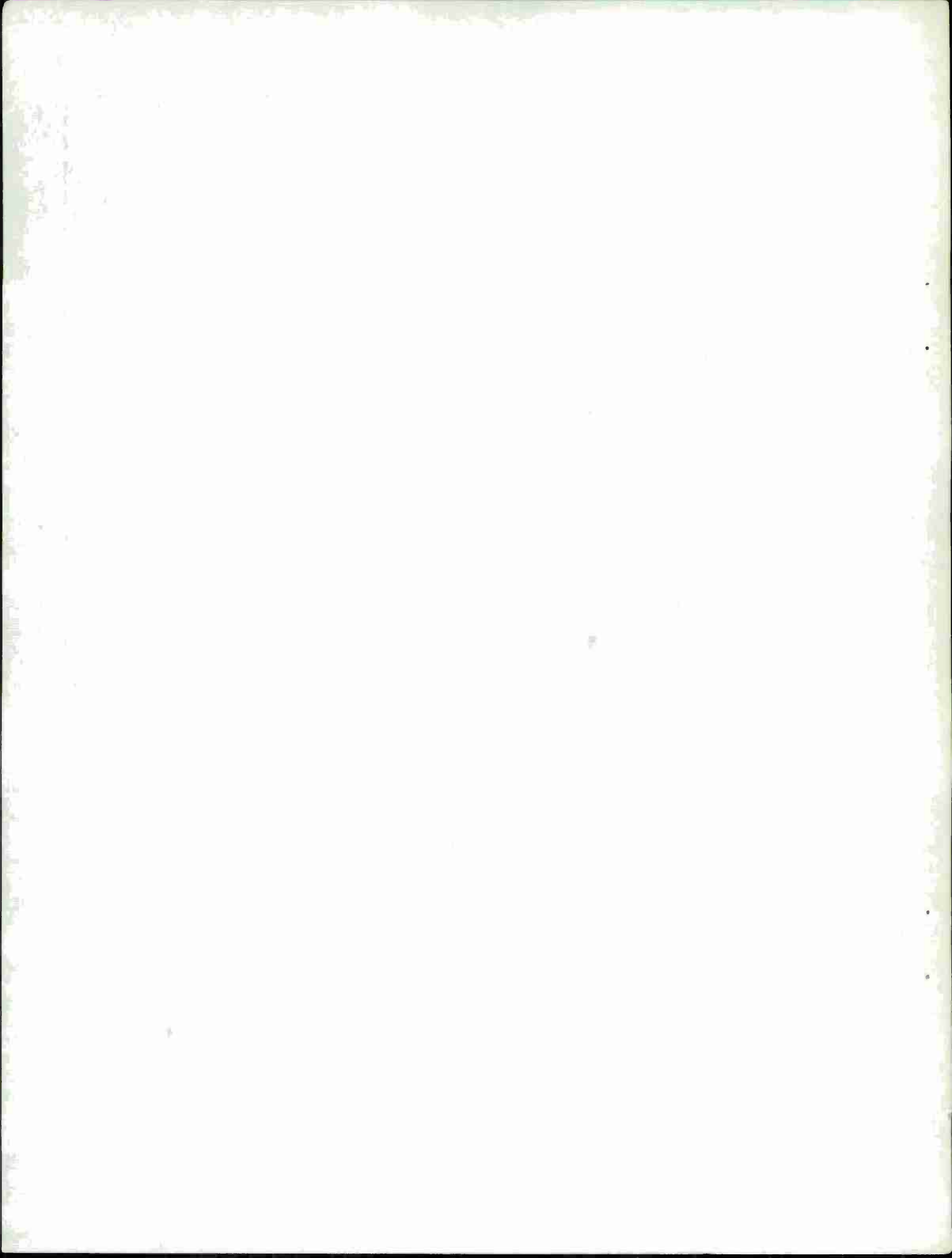
TABLE OF CONTENTS

Page

3

LIST OF ILLUSTRATIONS

5

I.   INTRODUCTION

This memorandum describes the present state of development of an ellipsoidal mirror reflectometer (EMR). The future application of the EMR is the measurement of the reflectance of heated metals at wavelengths emitted by powerful lasers. The metals to be emphasized are commercial aluminum and steel alloys, with known (measured) surface roughness.

For the intended application, a reflectometer able to gather all flux reflected, not just flux in a single direction, is needed. This reflectance may be used to infer the absorption of a material, a quantity of more importance to laser effects work. For any sample, incident flux is either transmitted, reflected, or absorbed. The sum of the ratios of each flux to the incident flux must be unity: T+R+A=1. This equation applies only when all reflected flux is collected by the reflectometer. With gas lasers flux is incident from essentially one direction. To emphasize these facts, R is best rewritten according to National Bureau of Standards (NBS) notation for directional-hemispherical reflectance

$$R \rightarrow \rho(\theta_o, \phi_o; 2\pi).^{1*}$$

Reflectometers which allow the evaluation of all flux from a reflecting sample are of two types: integrating sphere or imaging device. The former depends upon a coating which must be diffusing and highly reflective, and under the circumstances, stable under heat.

Coatings showing promise through the middle infrared have been reported;[2] but in a sphere coated with a commonly available substance the longest wavelength used, known to the authors, is 3.4 μm.[3] The integrating sphere coating diffuses reflected flux and the detector senses the wall brightness. In contrast, imaging reflectometers do not diffuse the flux but converge (image) the flux onto the detector. The flux that is imaged is just that which is reflected by the sample. The imaging device is a polished surface, usually metal, and therefore can image flux from visible to middle infrared spectral regions. Past instruments of the imaging type were polished hemispherical mirrors. Sample and detector were placed equally off-center and flux introduced to the sample through a hole in the mirror wall. The arrangement results in poor imaging with consequent errors caused by the detector's not sensing all flux and by its non-uniform sensitivity to off-axis flux.

An ellipsoidal mirror has the advantages over a hemispherical mirror of reduced image size and conveniently large spatial separation of sample and detector. The separation of components is important for accommodating bulky mounts and for heating the sample without affecting the detector.

---

*References are listed on page 17.

Sensitivity to off-axis flux is a problem not relieved by an EM, however.

II. DESCRIPTION OF MIRROR

1. Construction

The mirror design, Figure 1, was executed in the BRL shop by an unusual method shown schematically in Figure 2. A standard contour follower controlled a lathe cutting tool. A finger, which normally touches the outline of a template, was fixed to a point on a bar. One end of the bar moved in a track horizontally and the other end moved in a track vertically. The lathe was made to move the bar and the finger then moved on one quadrant of an elliptical path. The path generation was basically the draftsman's "long trammel" method of drawing an ellipse.[4] The error in making an ellipse template was entirely by-passed, leaving the (ever-present) control error of the follower over the cross-feed.

As a large block of aluminum was spun in the lathe, the cutting tool (at the end of a boring bar) followed the elliptical path the finger took. At completion of the cutting, the cavity formed a half-ellipsoid. The maximum depth was the length of the semi-major axis and the cavity opening was the diameter of the minor axis. This geometry meant that one focus lay inside the real cavity and the other focus lay inside the cavity of a phantom half-ellipsoid. To bring the foci into the plane of the cavity opening, the block was bisected (cut AA') and the two symmetrical halves rejoined as in Figure 3. Six holes were bored through the block. Three holes, axes coplanar, were centered on each focus, the axis of one normal to the cavity opening (now the focal plane) and the other two at 45°.

The cavity was given an initial polish while on the lathe. Afterwards hand polishing was done with grades of diamond paste on cotton. Each succeeding grade was swabbed out with acetone on cotton.

2. Imaging

The imaging equations are derived in Appendix A. Other authors have used other treatments. The equations are not simple relations involving only the ellipsoid dimensions. They are complicated by the appearance of the coordinates of the reflection point on the EM surface. Rays leaving the same source point are reflected to different spots depending on where on the EM they are reflected. The image of a finite sized source is a composite of the areal images of each radiating point in the source. The greatest extent of the image is the maximum

magnification of the EM times the source dimension. From Bradenberg[5] or equations A15 the maximum magnification for a small source centered at one focus is

$$M_x^{\,2} = \left[(a^2 + fa) \Big/ (a^2 - fa) \right]^2 = My \quad ,$$

where a is the length of the semi-major axis (axis of revolution of the ellipse) and f is the distance of the foci from the center of the ellipsoid. For our mirror the maximum magnification is 4.16 along the semi-major axis and 2.04 perpendicular to it.

Knowing the size of the image is of importance since the entrance aperture of the flux-collection apparatus must be large enough to admit all the imaged flux. For an EM the magnification is fixed by the length of the semi-major axis and the separation of the foci. But by keeping the irradiated area on the sample small, and centered on one focus, the image size is small and collection loss is minimized.

As an imaging test, a helium-neon laser beam was made to impinge normally on graph paper taped over the focal plane of the mirror. The paper was assumed to reflect the beam over all parts of the mirror. It also easily located the focal plane and directly gave the sizes of the incident and imaged spots.

Figure 4 shows that the ellipsoidal mirror image and object sizes are equal for a small object. The areas are larger than the laser beam diameter, 1 mm, due to a time exposure accenting the light scattered from paper and mirror, and inter-reflections of source and image which enlarge the area containing the flux. The diffraction pattern of the laser beam through a screen (1000 lines per inch) was also used as a source to be imaged by the EM. The photograph of Figure 5 shows that the EM does not image the areal pattern with fidelity. This illustrates the need to keep the irradiated area at one focus small.

3. Flux Losses

Several tests established the magnitude of flux loss of the EM. Losses can be expected from flux being reflected out the holes, and from absorption and scattering at the mirror surface. The mirror efficiency usefully expresses the loss. Efficiency is the ratio of detection apparatus signal with and without the EM. The signal with the EM is obtained by bringing flux onto a standard reflection target at one focus while the detector is at the other focus. The signal without the EM is measured by removing the standard target and placing the detector in the target position. The ratio of signals so obtained is unity for a perfect EM and less than unity for a real EM.

9

A standard target should be one with a known (preferably close to unity) reflectance. Four reflectors were tried: a flat (1/10 λ) aluminum coated front surface mirror, a magnesium oxide coating on nominally flat metal, a new ball-bearing, and a ball-bearing smoked with magnesium oxide.

The target, located at one focal point of the EM, reflected a helium-neon laser beam (1 mW) which the EM gathered to the other focal point. There, flux was detected by a silicon solar cell (100 Ω, 1 mV signal) attached to an averaging sphere. The sphere insured that detector saturation and angular sensitivity were not problems. The detector reading in this configuration was compared to the reading taken on the direct beam. The ratio of readings, divided by the true directional-hemispherical reflectance of the target, was the mirror efficiency. The flat mirror allowed individual small areas of the ellipsoidal mirror to be tested without hole loss. The round targets deviated flux (non-uniformly) over the entire 2π steradian collection solid angle of the mirror and thus hole loss could be included. Appendix B discusses the diameter of a shiny ball-bearing needed for a desired conical re-flection. For the laser beam, 2.8 mm sufficed. The whitened ball-bearing checked the assumption that a new ball-bearing has 100 percent reflectance. The assumption was wrong as comparison of the measurements led to a directional-hemispherical reflectance of 0.58 for a shiny ball-bearing. Table 1 gives the efficiency of the EM as found by a flat mirror, a whitened flat, and a whitened ball-bearing.

Table 1   Ellipsoidal Mirror Efficiency, 633 nm

	Flat Mirror*	Whitened Flat	Whitened Ball-Bearing
Efficiency	0.59	0.38	0.39

*There is no hole loss with this target, so the efficiency is actually the directional-hemispherical reflectance of the EM surface.

4. Systematic Errors

There are certain systematic errors when reflected flux is measured in an EMR. They are induced by hole losses, interreflections of target and averaging sphere, and misalignment of target. Having the foci lie side-by-side instead of fore-and-aft prevented one error. The sample and its holder cannot block any reflected flux from the averaging sphere.

Hole losses can be the most serious error source in our EMR. The construction section described the holes as centered 0° and ±45° on each

10

focal point. The flux-admitting holes are one inch diameter the others
are half-inch diameter. There is always a hole in the specular direction
and with a properly aligned, polished sample most of the reflected flux
will pass out of the EM. Deliberate misalignment of a highly polished
target can greatly reduce hole loss. Imaging is worsened, but not flux
collection, if the averaging sphere entrance port accepts all the image.
With rougher targets a unidirectional lay combined with a tilt will con-
trol the reflection sufficiently to miss the holes. Details of this
technique are found under sample preparation in Section IV, page 14.

Interreflections are caused by flux in the averaging sphere being
back-reflected to the EM, which focuses it onto the target, which in
turn reflects it back to the mirror, and back to the averaging sphere.
The process repeats but the interreflected flux becomes weaker on each
pass due to the multiplicative factors of the mirror's reflectance and
the target's reflectance. The net effect is that the detector senses
more flux in the averaging sphere than would otherwise be there if there
were no interreflections.

Dunn, et. al.[6] give as the interreflection factor:

$$\left(1 - \rho_{hs}(\bar{\rho}_\varepsilon)^2_d \eta' f_{s-\varepsilon} \right)^{-1}$$

where ρ_{hs} is the hemispherical reflectance of the sample, $(\bar{\rho}_\varepsilon)_d$ is the
average effective reflectance of the mirror for flux coming diffusely
from the sphere entrance, η' is the fraction of flux back-reflected from
the sphere entrance aperture, and $f_{s-\varepsilon}$ is the fraction of the
back-reflected flux that the mirror intercepts and focuses on the sample.
If the factors in the denominator are close to unity, the whole term
will be very large and interreflections will have a significant effect.

To estimate the magnitude we take the reflectances of the mirror
$(\bar{\rho}_\varepsilon)_d$ and target (ρ_{hs}) to be 0.6 and 0.7. The fraction of back-reflected
flux η' is discussed in Appendix C. $\eta' = 0.37$. We assume the mirror
intercepts all back-reflected flux, $f_{s-\varepsilon} = 1$. Evaluating the inter-
reflection factor with these values gives 1.10, or a reading 10 percent
higher than if there were no interreflections.

11

III. AVERAGING SPHERES

Studies of the National Bureau of Standards[2] have emphasized that serious measurement errors may arise when radiation flux is incident off-axis and on different portions of a detector's sensitive area. These defects of detectors are termed angular and areal sensitivity. In our EMR the problems are acute since some rays are incident at large angles on a detector whose area is larger than the focused flux. The problems are corrected by using an averaging sphere. This device has a spherical interior with a diffusing coating of high reflectance. The distinction between averaging and integrating spheres is mostly functional. The former term is reserved for a device that corrects detector response and the latter term is reserved for a reflectometer. In addition, an integrating sphere would have more ports and light shields.

Two averaging spheres of different design have been tested for use with the EMR. In one the interior is unobscured by radiation shields and in the other the detector is shielded. In neither type can the detector receive flux directly but only flux reflected from the surface within the field of view. In the shieldless sphere, the detector is recessed from the sphere wall thus preventing any but internally re-flected flux from stiking it. The shielded sphere followed a design of Larche and Schulze[7]. The working design of the spheres is shown in Figures 6 and 7.

Flux enters through a port and is multiply reflected so that the sphere wall is of constant brightness. Through another port the detector views an area of the wall. As with the integrating sphere the averaging sphere has the drawback that coatings for the infrared have various in-adequacies. Another large problem is that averaging spheres are in-herently inefficient. An NBS analysis[2] shows that the efficiency, the ratio of detected flux to direct flux, can be expected to be 3 percent.

An averaging sphere would remove the effects of the geometric distribution of flux and cause the detector signal to be uniquely associated with one flux level. A sphere is tested with a certain mode of illumination. The sphere must be mounted to turn about an axis in the plane of the aperture. As it is turned the effective aperture area decreases as cosine θ. With the aperture fully and evenly illuminated from one direction, the quantity of flux admitted to the sphere will decrease as cosine θ. Then if there is no angular dependence, the detector output will also decrease as cosine θ.

In another mode of illumination, the aperture admits a beam whose diameter is small compared with that of the aperture. In effect this

12

test requires a light ray or its approximation, a HeNe laser beam. Now as the sphere is turned the admitted flux is constant and, if there is no angular dependence, the detector signal is constant. The tests are not equivalent. If a sphere-detector responds correctly to narrow-beam illumination, it will to full-beam illumination also. The converse is not true.

Figures 8, 9, and 10 show the response of the unshielded sphere and Larche-Schulze sphere to full and narrow illumination. On polar paper the desired responses are: a circle with maximum amplitude at normal incidence and zero amplitude at ±90° for full illumination and a semi-circle centered on the origin for narrow illumination. For the unshielded sphere the measured response is within 17 percent of the ideal response over the angular limits of ±70°, set by the finite size of the laser beam and wall thickness of the sphere entrance port.

The Larche-Schulze sphere was designed for ultraviolet skylight measurements, i.e., aperture fully, evenly, and hemispherically illuminated. When tested for cosine fall-off of response, the sphere did give good results. However, when tested for a semi-circular response it did not. The reason is that a narrow beam (semi-circular response) has the effect of probing the internal structure. The shield reflects to the wall a large portion of normally incident flux; all flux incident beyond ±30° strikes the wall directly. The increased response beyond ±30° is explained by there being one less internal reflection for these angles, and not good diffusion.

The measurement error caused by angular sensitivity is not known. It should be assumed that very different flux distributions, as from scratched target and smooth reference mirror, will cause a large error. Similar flux distributions would cause the least error.

IV.   TARGETS

The EMR will accept flat targets of any material. However, the intention is to use metal targets which are externally heated. The targets are one inch by one inch right cylinders machined out of commercial aluminum (2024-T4, 6061-T6, 7075-T6) and steel (1020; 1085 ST, 4140 ST) alloys. A blind hole 3/4 inch diameter is drilled in one end; the hole allows a propane torch flame to melt the front end within several minutes. Also, 1/16 inch behind the reflecting end are holes for two thermocouple probes. The target rests against set screws in an open-ended cylindrical holder. A gas fitting at the front end of the holder permits a non-absorbing, non-reacting gas, such as argon, to flow over the reflecting end of the target. The target holder is joined by a rod to a positioning assembly with fine angular and translational control.

The mounted target, seen from the reflecting side, is shown in Figure 11.

13

Tool marks must be removed before reflection measurements can be made. Surface preparation consists of hand rubbing the reflecting face against successively finer grades of silicon carbide paper. The target is "dropped in" to form part of the flat face of a 4-inch diameter polishing jig. Rubbing back and forth on glass-backed, wetted paper produces a unidirectional lay. At the next finer paper the jig is turned 90° and rubbing continues until only new scratches are seen. The final surface is one which is scratched by a particular grade of paper. We have ended with 320 or 600 grade paper. A higher polish can be given aluminum targets with 800 grit slurry, a rinse, and then a magnesium oxide slurry on a felt covered polishing wheel.

The lay causes reflected flux to be contained in a fuzzy band lying symmetrically about the specular direction. A picture of the band, from a HeNe laser beam, and a magnified portion of the target are shown in Figures 12 and 13.

Diffraction probably causes the band. The unidirectional scratches on the metal form a poor quality reflection grating. Diffraction orders are not seen, as they would be with numerous, regularly spaced grooves; but, as with diffraction, the band is perpendicular to the direction of the scratches, i.e., horizonally running scratches cause the band to be vertical. Confinement of the reflected flux to a band and control over the specular direction allow relatively little flux to fall on a hole in the EM and be lost. Low hole loss can also be achieved with highly polished targets. However, the surface finish is then better than that of real targets of interest.

V. COMPARISON WITH REFLECTOMETER IN NIR

Near infrared (NIR) reflectance measurements of a room-temperature target were made with the EMR and a Beckman DK-2A reflectometer. The EMR apparatus is shown by a block diagram and a photograph in Figures 14 and 15. The target was Al 2024-T4 scratched unidirectionally on No. 600 silicon carbide paper. A combination of tilt and diffraction from sur- face lay visibly minimized hole loss. The source was a tungsten-halogen lamp designed as a standard irradiance source and powered by a constant current supply (Optronic Laboratories). The filament is spiral wound, 2 in. x 1/4 in. in size. Lamp flux was spectrally filtered and chopped (13 Hz) before it entered the EMR. Two quartz lenses (3 in. and 2 in. diameter) cast a demagnified image of the filament onto the target at the EM focal plane. The corresponding image at the averaging sphere's entrance port was 7/8 in x 1/8 in. The averaging sphere was slightly tilted so that the entrance port best admitted the imaged flux. The detector was from a Spectra-Physics Model 4018 power meter. Detector voltage was preamplified (x10 gain) before being synchronously amplified (x10 gain) and further amplified by an oscilloscope where the ac signal was monitored. A proportional ac signal, available at the oscilloscope, was rectified and sent to an xy recorder and digital voltmeter (DVM).

The recorder was used to verify system stability (half hour warm-up needed); data were taken from the DVM.

DVM readings were made sequentially with eight narrowband (0.01 μm) filters from 0.8 μm to 1.5 μm, then repeated twice more. The reference mirror was then put in place and, along with the averaging sphere positioned for negligible hole loss and most flux collection. The DVM readings were made as before. The mean target reading was divided by the mean reference mirror reading and the result multiplied by the spectral reflectance of the reference mirror (obtained with the Beckman DK-2A).

VI. RESULTS

The reflectance from the same sample was measured on three different days. The graph, Figure 16, shows the results individually. Data of 25 and 28 June are close compared to those of 24 June. In each run the only variable is the positioning of target, reference mirror, and averaging sphere so this factor is the probable cause of spread among the curves. The calculated reflectance at each wavelength was averaged and an estimate of the standard deviation was made from the range, a method appropriate to small sample populations.[8]

The spectral reflectance recorded by three runs on the DK-2A was averaged and the sample estimated standard deviation computed. The averages of the three runs of both instruments are shown in Figure 17. The averaged data for the Beckman and for the EMR are listed in Tables 2 and 3 along with the percentage disagreement between the instruments.

From 0.8 μm to 1.5 μm the estimate of the standard deviation for the EMR is 0.042 and for the Beckman DK-2A it is 0.006. The average disagreement is 16 percent. This disagreement is perhaps not typical of what is obtainable with unscratched specimens. It was repeatedly seen that the Beckman reading changed radically when the scratched target was rolled around its cylindrical axis. By looking into the integrating sphere when the spectophotometer was admitting visible radiation, the aforementioned diffraction band could be seen. A maximum reading (over 100 per cent) occurred with the band falling between the slits with noticeable flux also falling in the field of view of the detector. A minimum reading (those reported for comparison with the EMR) occurred when the diffraction band fell across the entrance slits of the integrating sphere and outside the field of view of the detector. So the Beckman reading would have higher hole loss than the EMR. The comparison plot in Figure 17 does show the Beckman reading everywhere lower than the EMR. The reliable figure of the comparison is thought to be the data scatter that each instrument produces; the Beckman is seven times as good as the EMR in this regard.

15

VII. CONCLUSION

The EMR is intended for operation at wavelengths of high power lasers, i.e., the middle infrared. It was instrumented for a reflectance test in the near infrared in order to compare its accuracy and precision with those of a commercially available reflectometer in the working range of the latter instrument. Results showed a 16 percent offset with EMR reading higher; the data scatter was seven times as high with the EMR. Both instruments are sensitive to the reflectance pattern off a unidirectionally scratched surface. This type of surface preparation avoided flux loss through holes in the EM.

Measurement with the EMR requires the reflector to be slightly tilted to avoid hole loss and the averaging sphere to be positioned where the image is smallest. The incident flux is determined by a high quality mirror. Again careful alignment of reflector and collector is needed. Also, the source of flux must have constant output during the time needed to complete the measurements. The data scatter may be largely due to the positioning routine.

Presumably the data scatter reported here would be the same in the middle infrared; the reflectance itself of metals is higher there than in the near infrared. The averaging sphere belonging with the EMR causes major difficulty in the middle infrared. Equipment threatening flux levels are needed for adequate signal when the present averaging sphere is used with a thermopile detector. Output response to off-axis flux has also been non-ideal. A sphere coating with reflecting and diffusing properties superior to shot-blasted aluminum is needed. A coating of gold, evaporated over the present rough surface, would probably be suitable.

In the middle infrared there are operating advantages in leaving the metal target surface unscratched. A moderate polish gives a sufficiently specular reflectance pattern that, together with tilt, hole loss is avoided. Accuracy would be acceptable, contingent on an improved averaging sphere. Precision would be improved since the target positioning routine would be less critical than with the scratched target. Finally, if the emphasis were to be put on changes of reflectance from a hot target, rather than magnitude of reflectance, the EMR would serve very well.

REFERENCES

1. Judd, Deane B., Terms, Definitions, and Symbols in Reflectometry, J. Opt. Soc. Am. 57, 445 (1967).

2. Richmond, Joseph C., and Geist, Jon C., Infrared Reflectance Measurements, NBS 10071 (1969).

3. Kneissl, G. J., and Richmond, J. C., A Laser-Source Integrating Sphere Reflectometer, NBS, TN 439 (1968).

4. Giesecke, F. E., Mitchell, A., Spencer, H. C., and Hill, I. L., Technical Drawing, New York, Macmillan Co., 5th Ed., p112, (1967)

5. Brandenberg, W. M., Focusing Properties of Hemispherical and Ellipsoidal Mirror Reflectometers, J. Opt. Soc. Am. 54, 1235 (1964).

6. Dunn, S. Thomas, Richmond, J. C., and Wiebelt, John A., Ellipsoidal Mirror Reflectometer, J. Res. NBS, 70C, 82 (1966).

7. Larche, K. and Schulze, R., On An Instrument For The Measurement of Ultraviolet Radiation Equipped With A Spherical Attachment For The Measurement of Radiation Incident At A Large Angle, NASA TT F-14418 (1972).

8. Experimental Statistics (Section 1), AMCP 706-110, p2-6 (1969).

9. Heinisch, R.P., Anderson, J. K., Schmidt, R. N., Emittance Measurement Study, NASA CR-1583, p53 (1970).

10. Weatherburn, C. E., Elementary Vector Analysis, G. Bell and Sons, Ltd., London, p23, (1946).
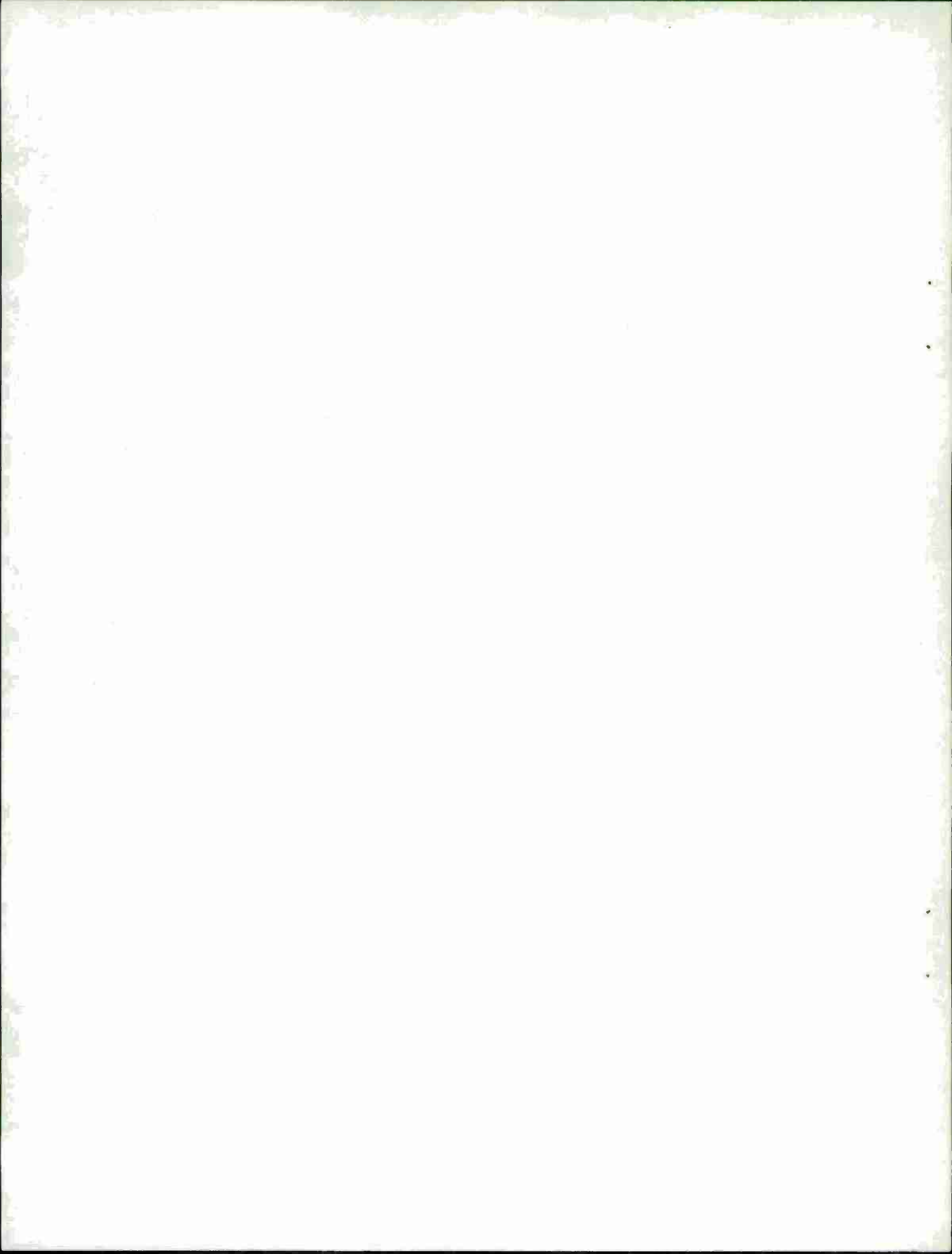
APPENDIX A

OUTLINE OF DERIVATION OF FOCUSING PROPERTIES

OF AN ELLIPSOIDAL MIRROR

While the results to be obtained here are not new, the method is free of ambiguities found in previous derivations. The method is quite different from any known previous derivation and is straightforward.

We take the hemiellipsoid to be of the form

$$\frac{x^2}{b^2} + \frac{y^2}{a^2} + \frac{z^2}{b^2} = 1 \tag{A1}$$

with $a > b$ so that the y axis is the major axis. Then at a point on the ellipsoid (x_2, y_2, z_2) the normal is given by

$$\vec{n} = \frac{2x_2}{b^2} \, \hat{i} + \frac{2y_2}{a^2} \, \hat{j} + \frac{2z_2}{b^2} \, \hat{k} \quad . \tag{A2}$$

Referring to Figure A1, the vector from the origin (position vector) to some point on the normal vector is

$$\vec{r} = \vec{r}_{02} + \vec{n}$$

$$\vec{r} = x_2 \, \hat{i} + y_2 \, \hat{j} + z_2 \, \hat{k} + s \, \vec{n} \tag{A3}$$

where s is a parameter and can have any value; each value corresponds to some point on the normal.

A ray trace through the hemiellipsoid, showing parameters needed later, is presented in Figure A2[9].

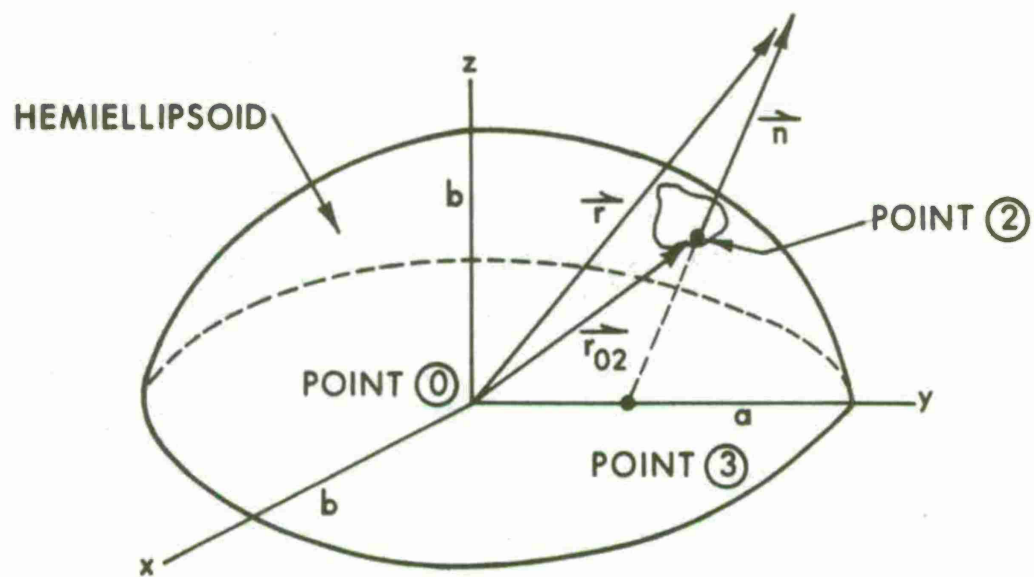We now envision a source point $(x_1, y_1, 0)$ from which a ray
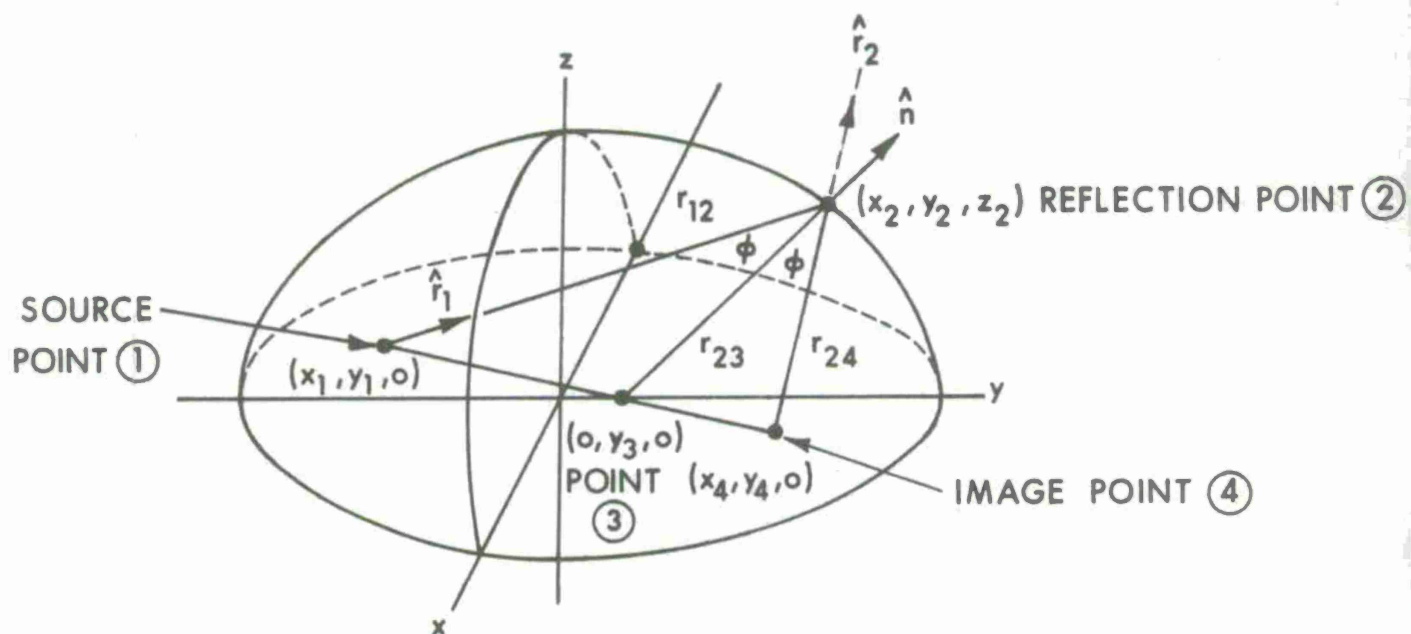
Figure A1. Position Vector of Ellipsoid Normal

Figure A2.   Ray Tracing for a Hemiellispoid

strikes the ellipsoid at (x_2, y_2, z_2) and is reflected through the point $(x_4, y_4, 0)$. The source and image points are taken in the plane $z = 0$. The intersection of the normal to the ellipsoid with the plane $z = 0$ is denoted by $(x_3, y_3, 0)$. To determine this point we have

$$\vec{r} = x_3\,\hat{i} + y_3\,\hat{j} = x_2\,\hat{i} + y_2\,\hat{j} + z_2\,\hat{k} + s\left(\frac{2x_2}{b^2}\,\hat{i} + \frac{2y_2}{a^2}\,\hat{j} + \frac{2z_2}{b^2}\,\hat{k}\right) \cdot \quad (A4)$$

From this we obtain

$$x_3 = 0 \qquad ,$$

$$y_3 = \frac{y_2}{a^2}\,f^2 \qquad , \qquad\qquad (A5)$$

where

$$f^2 = a^2 - b^2 \qquad .$$

We wish to determine the coordinates of the image point $(x_4, y_4, 0)$. To do this we must first find the equation of the reflected ray. This is determined by the condition that the surface normal bisect the angle between the incident and reflected rays. Denote the direction of the incident ray by $\hat{r}_1$, the direction of the normal by $\hat{n}$, and the direction of the reflected ray by $\hat{r}_2$. The circumflex $\wedge$ signifies a unit vector.

$$\hat{n} = q\,(\hat{r}_1 + \hat{r}_2) \qquad ,$$

$$\qquad\qquad (A6)$$

and since $\hat{n}.\hat{n} = 1$,

$$q = \left[\frac{1}{2\,(1 + \cos 2\phi)}\right]^{1/2} \qquad ,$$

22

where ϕ is the angle between the incident ray and the surface normal and 2ϕ is the angle between the incident and reflected rays.[10] Then

$$\hat{r}_2 = \left[2 \left(1 + \cos 2 \phi \right) \right]^{1/2} \hat{n} - \hat{r}_1 \quad ,$$

$$\hat{r}_1 = \frac{(x_2 - x_1) \hat{i} + (y_2 - y_1) \hat{j} + z_2 \hat{k}}{\left[\left(x_2 - x_1 \right)^2 + \left(y_2 - y_1 \right)^2 + z_2^2 \right]^{1/2}} \quad , \tag{A7}$$

$$\hat{n} = \left(\frac{x_2}{b^2} \hat{i} + \frac{y_2}{a^2} \hat{j} + \frac{z_2}{b^2} \hat{k} \right) \cdot \left[\frac{x_2^2}{b^4} + \frac{y_2^2}{a^4} + \frac{z_2^2}{b^4} \right]^{-1/2} \quad .$$

We take the position vector of some point on the reflected ray to be

$$\vec{r}_2 = x_2 \hat{i} + y_2 \hat{j} + z_2 \hat{k} + s \hat{r}_2 \quad , \tag{A8}$$

where s takes on all real values. We wish the intersection of this line with the plane $z = 0$, i.e., the image point, $(x_4, y_4, 0)$. At this point

$$\vec{r}_2 = x_4 \, \hat{i} + y_4 \, \hat{j}$$

$$= x_2 \, \hat{i} + y_2 \, \hat{j} + z_2 \, \hat{k} + s \left\{ \left[\frac{2 \, (1 + \cos 2\phi)}{\left[\dfrac{x_2^2}{b^4} + \dfrac{y_2^2}{a^4} + \dfrac{z_2^2}{b^4} \right]^{1/2}} \right]^{1/2} \left(\frac{x_2}{b^2} \, \hat{i} + \frac{y_2}{a^2} \, \hat{j} + \frac{z_2}{b^2} \, \hat{k} \right) \right.$$

$$\left. - \frac{(x_2 - x_1) \, \hat{i} + (y_2 - y_1) \, \hat{j} + z_2 \, \hat{k}}{\left[\left(x_2 - x_1 \right)^2 + \left(y_2 - y_1 \right)^2 + z_2^2 \right]^{1/2}} \right\} . \tag{A9}$$

Now let s_4 be the value of the parameter s for which the reflected ray intersects the $z = 0$ plane. We can then solve the preceding equation for s_4 by equating the $\hat{k}$ component to zero. Doing this yields

$$s_4 = \left\{ \left[\left(x_2 - x_1 \right)^2 + \left(y_2 - y_1 \right)^2 + z_2^2 \right]^{-1/2} \right.$$

$$\left. - \left(2 + 2 \cos 2\phi \right)^{1/2} \middle/ b^2 \left(\frac{x_2^2}{b^4} + \frac{y_2^2}{a^4} + \frac{z_2^2}{b^4} \right)^{1/2} \right\}^{-1} . \tag{A10}$$

Substituting s_4 back into equation A9 and separately collecting $\hat{i}$ and $\hat{j}$ components, yields equations for x_4 and y_4. The equations contain the angle ϕ explicitly. It can be eliminated but the algebraic details are tedious so the operations will only be indicated. Referring to Figure A2, we symbolize distances between points by a subscripted r, e.g.,

24

the separation of point 1 and point 2 is r_{12}. Then by the law of
cosines, $r_{13}^2 = r_{12}^2 + r_{23}^2 - 2r_{12} \, r_{23} \cos \phi$,

so we have

$$(2 + 2 \cos 2\phi)^{1/2} = \left(r_{12}^2 + r_{23}^2 - r_{13}^2 \right) \Big/ r_{12} \, r_{13} \, . \qquad (A11)$$

Application of the hemiellipsoid relations A1 and A5 and the usual
distance formula e.g.,

$$r_{12} = \left[(x_2-x_1)^2 + (y_2-y_1)^2 + z_2^2 \right]^{1/2} , \qquad (A12)$$

finally bring the equations for x_4 and y_4 into the following form:

$$x_4 = x_1 \frac{a^4 - f^2 y_2^2}{2 a^2 \left[y_1 y_2 + x_1 x_2 \frac{a^2}{b^2} \right] - \left(a^4 + f^2 y_2^2 \right)} , \qquad (A13)$$

$$y_4 = \frac{y_1 \left(a^4 + f^2 y_2^2 \right) + 2 a^2 f^2 y_2 \left[\left(x_1 x_2/b^2 \right) - 1 \right]}{2 a^2 \left[y_1 y_2 + \frac{a^2}{b^2} x_1 x_2 \right] - \left(a^4 + f^2 y_2^2 \right)} .$$

These are the desired equations for the image point. While the deri-
vation is tedious it is free of ambiguities which arise in previous
procedures which involve simultaneous solution of sets of quadratic
equations.

Using the equations for the image coordinates x_4, y_4, we can find
the changes in image coordinates with change in source coordinates.
The needed derivatives are $\frac{\partial x_4}{\partial x_1}$, $\frac{\partial x_4}{\partial y_1}$, $\frac{\partial y_4}{\partial x_1}$, $\frac{\partial y_4}{\partial y_1}$, but, as they are not

25

simple expressions, only the first will be written out.

$$\frac{\partial x_4}{\partial x_1} = \frac{(a^2 - fy_2)\ (a^2 + fy_2)\ \left[-a^4 + 2a^2\ y_1\ y_2 - f^2\ y_2^2 \right]}{\left[a^4 - 2a^2\ y_1\ y_2 + f^2\ y_2^2 - \dfrac{2a^4}{b^2}\ x_1\ x_2 \right]^2} \quad . \quad (A14)$$

The physical meaning of the first partial derivative is that it gives the change in the x coordinate of the image point as the x coordinate of the source point is changed. A similar interpretation applies to the other partial derivatives. At the source point $(x_1, y_1) = (0, -f)$ the derivatives do take a simple form.

$$\left. \frac{\partial x_4}{\partial x_1} \right|_{(0,-f)} = -\left(\frac{a^2 - fy_2}{a^2 + fy_2} \right) \quad ,$$

$$\left. \frac{\partial x_4}{\partial y_1} \right|_{(0,-f)} = 0 \quad ,$$

$$(A15)$$

$$\left. \frac{\partial y_4}{\partial x_1} \right|_{(0,-f)} = \frac{2a^2\ fx_2\ (a^2 - fy_2)}{b^2\ (a^2 + fy_2)^2} \quad ,$$

$$\left. \frac{\partial y_4}{\partial y_1} \right|_{(0,-f)} = -\left(\frac{a^2 - fy_2}{a^2 + fy_2} \right)^2 \quad .$$

The first and fourth of these equations are Brandenberg's magnification equations referred to in the text, page 9. The expressions only hold with respect to a small region about the source point when it is at one focal point of the ellipsoid. The algebraic sign of the magnification is of no consequence.

26

Displacements of the source point of magnitude dx_1, dy_1 result in image point displacements of

$$\left(\frac{\partial x_4}{\partial x_1} \hat{i} + \frac{\partial y_4}{\partial x_1} \hat{j} \right) dx_1$$

and   (A16)

$$\left(\frac{\partial x_4}{\partial y_1} \hat{i} + \frac{\partial y_4}{\partial y_1} \hat{j} \right) dy_1, \qquad \text{respectively,}$$

where $\hat{i}$ and $\hat{j}$ are unit vectors in the x_4 and y_4 directions and where the reflecting point on the ellipsoid surface is held fixed. The differential source area is imaged on an area whose magnitude is that of the vector product of the above two displacements. Taking the magnitude of the vector product yields, using the second of equations A15,

$$\left| \overrightarrow{dA_4} \right| = \frac{\partial x_4}{\partial x_1} \frac{\partial y_4}{\partial y_1} \, dx_1 \, dy_1 \ . \qquad (A17)$$

The areal magnification is then

$$M = \frac{dA_4}{dx_1 dy_1} = \frac{\partial x_4}{\partial x_1} \frac{\partial y_4}{\partial y_1} = \left(\frac{a^2 - fy_2}{a^2 + fy_2} \right)^3 \ . \quad (A18)$$

(This expression is just equal to the Jacobian of the transformation connecting the source coordinates x_1, y_1, with the image coordinates x_4, y_4).

The areal magnification is independent of x_2, z_2. An object space rectangle becomes in image space a parallelogram whose shape depends upon all coordinates needed to specify a ray direction. For the case in which a and b are "almost" equal, f is "small" so that an object space rectangle becomes an "almost" rectangular shaped parallelogram in image space for any fixed ray direction.

27
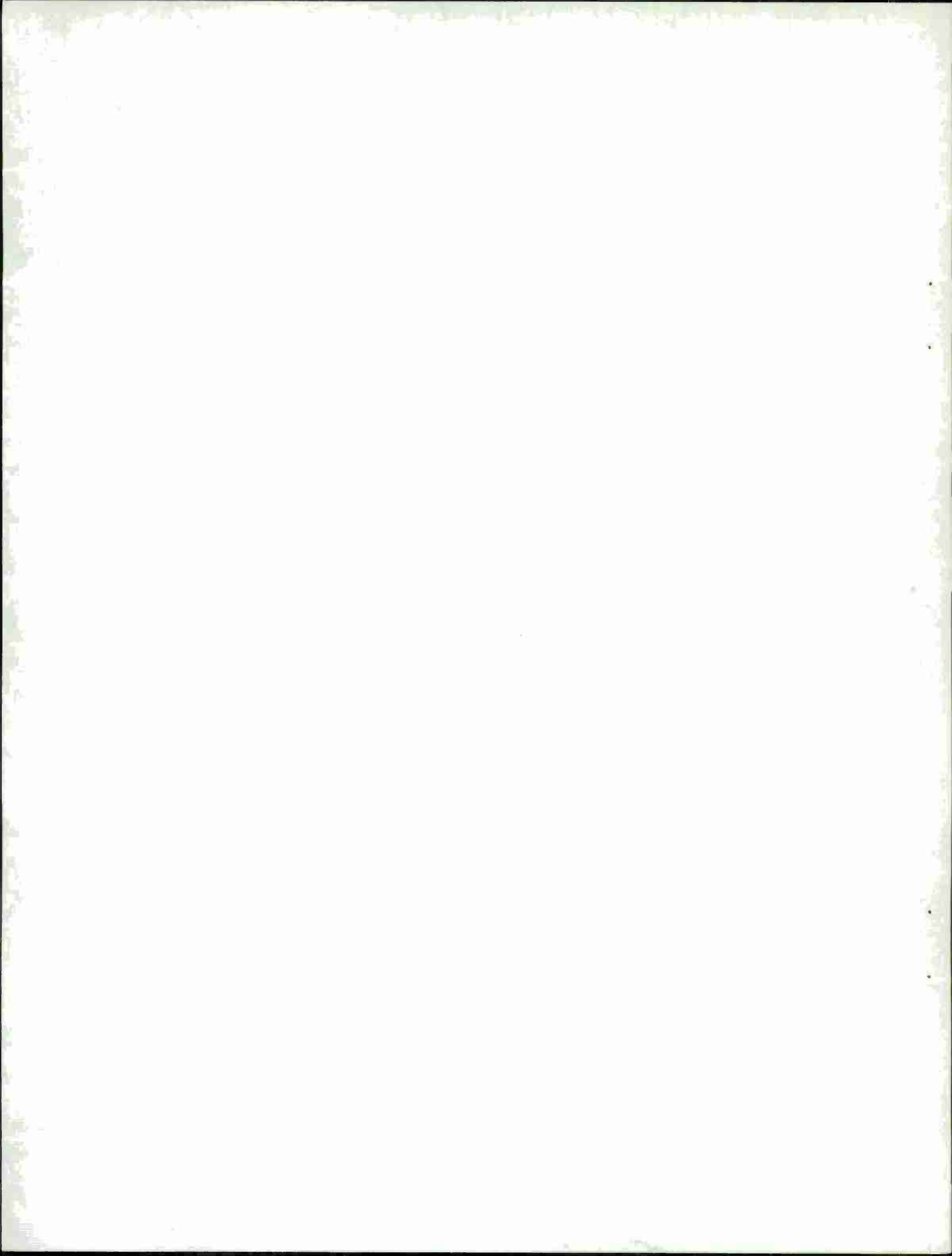
APPENDIX B

DEVIATION OF LASER BEAM FROM A BALL-BEARING

A ball-bearing deviated a HeNe laser beam 180°, filling the ellipsoidal mirror. The required size of the ball is found with the aid of Figure B1.
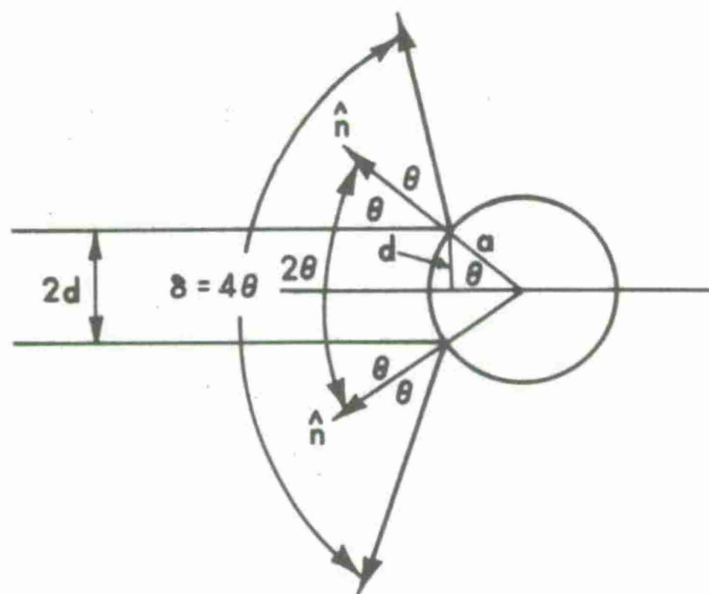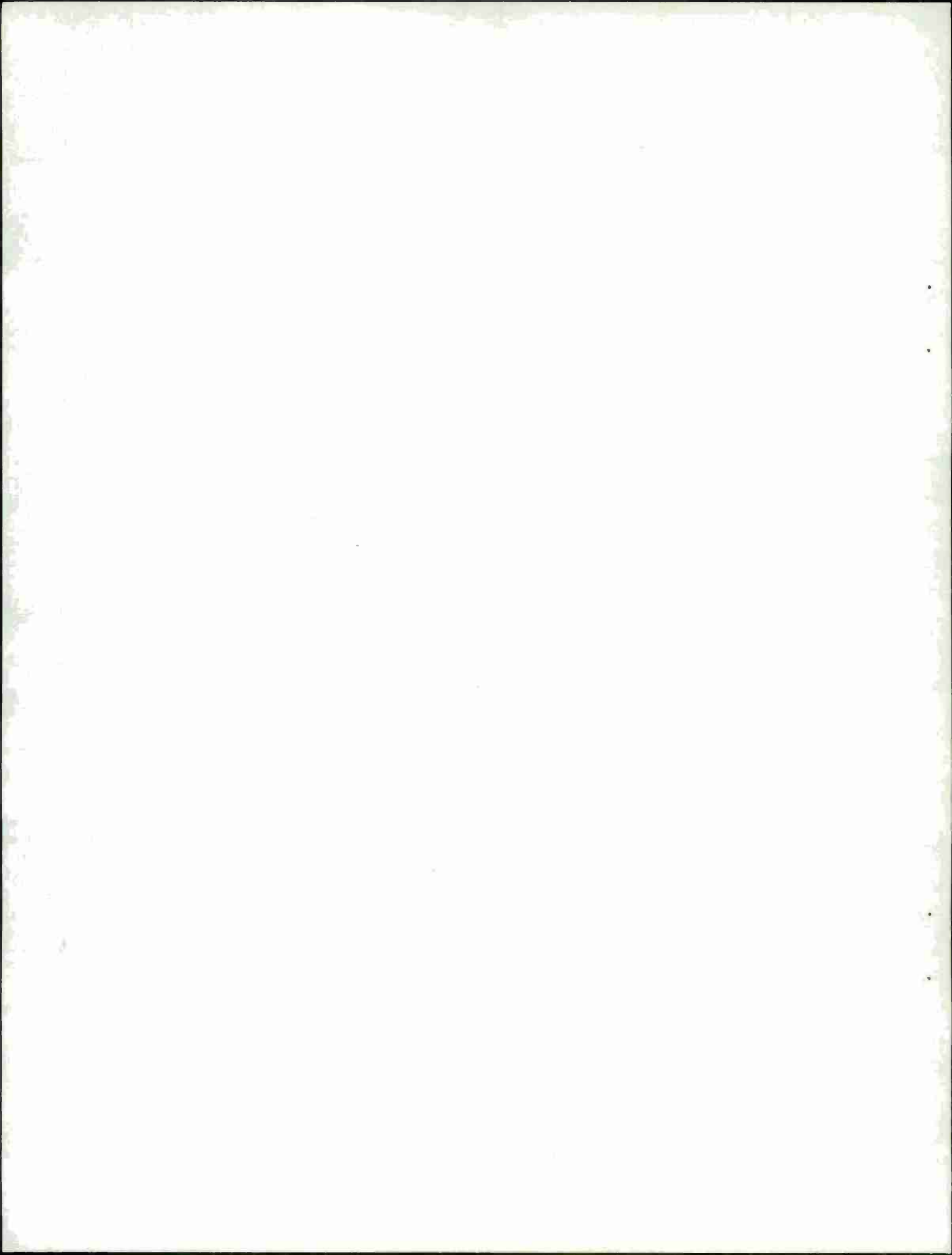

Figure B1.   Deviation of Laser Beam from a Ball-Bearing

The beam is collimated and of diameter 2d. The ball-bearing, of radius a, deviated the beam through an angle δ,

$$\delta = 4\theta \quad ,$$

$$\theta = \arcsin\left(\frac{d}{a}\right) \quad .$$

For a deviation of 180°, beam 2 mm diameter, the ball-bearing should be 2.8 mm diameter.

APPENDIX C

BACK-REFLECTIONS FROM AN AVERAGING SPHERE

An averaging sphere is drawn in Figure C1.

ϕ_e = back-reflected flux

ϕ_o = entering flux

A = sphere area

A_d = detector port area

A_e = entrance port area

ρ_w = wall reflectance

( ) = $(1-A_e/A-A_d/A)$, quantity proportional to flux remaining in sphere after port losses
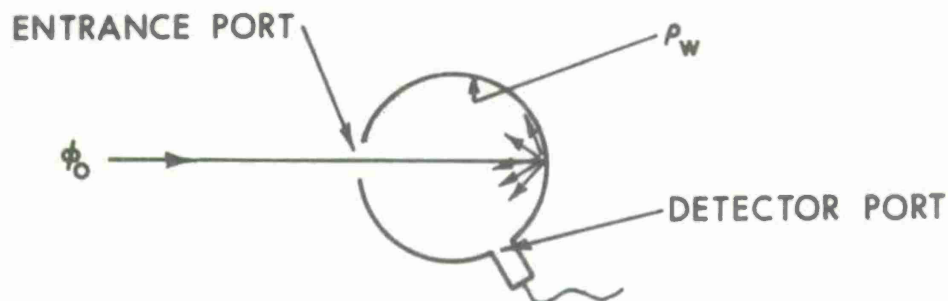

Figure C1. Averaging Sphere Geometry

The total flux passing out of the entrance port is called the back-reflected flux. The analysis follows that of Richmond and Geist.[2] The flux in the sphere after the first reflection is $\phi_o\rho_w$. Assuming the coating is a perfect diffuser, the fraction of this flux falling on the entrance is A_e/A. The flux remaining in the sphere after the two port losses (detector port and entrance port) is $\phi_o\rho_w$ $(1-A_e/A-A_d/A)$.

The flux is reduced by reflection on A, of which the fraction falling on the entrance port is A_e/A. The flux that has passed out due to two reflections, from the initial spot and from the whole area, is

$$\phi_o \rho_w^2 \ (1-A_e/A-A_d/A) \ A_e/A \rightarrow \phi_o \rho_w^2 \ A_e/A \ (\quad).$$

The argument continues for successive reflections. An accounting of flux loss is shown in Table C1, which reads left to right.

<p align="center">Table C1.   Flux Account</p>

| Reflec-tion	Flux in sphere	Flux Out Entrance Port	Flux in sphere after port losses
1	$\rho_w \phi_o$	$\rho_w \phi_o A_e/A$	$\rho_w \phi_o \ (\ )$
2	$\rho_w^2 \phi_o \ (\ )$	$\rho_w^2 \phi_o \ (\ ) A_e/A$	$\rho_w^2 \phi_o \ (\ )^2$
3	$\rho_w^3 \phi_o \ (\ )^2$	$\rho_w^3 \phi_o \ (\ )^2 A_e/A$	$\rho_w^3 \phi_o \ (\ )^3$
...	...	...	...
n	$\rho_w^n \phi_o \ (\ )^{n-1}$	$\rho_w^n \phi_o \ (\ )^{n-1} A_e/A$	$\rho_w^n \phi_o \ (\ )^n$

Summing the terms in the third column gives the back-reflected flux.

$$\phi_e = \phi_o \ (\rho_w A_e/A) \left[1 + \rho_w \ (\ ) + \rho_w^2 \ (\ )^2 + \ldots + \rho_w^n (\ )^n \right].$$

Summing the infinite series gives

$$\phi_e/\phi_o = (\rho_w A_e/A) \left[\cfrac{1}{1 - \rho_w\left(\cfrac{1-A_e}{A} - \cfrac{A_d}{A}\right)} \right] .$$

For our four inch diameter sphere, $A_e/A = 0.035$ and $A_d/A = 0.006$. The wall reflectance can be 0.95 for MgO. With these figures, $\phi_e/\phi_o = 0.37$ or 37 percent of the entering flux is back-reflected. The ratio ϕ_e/ϕ_o is called η' in the text, page 11.
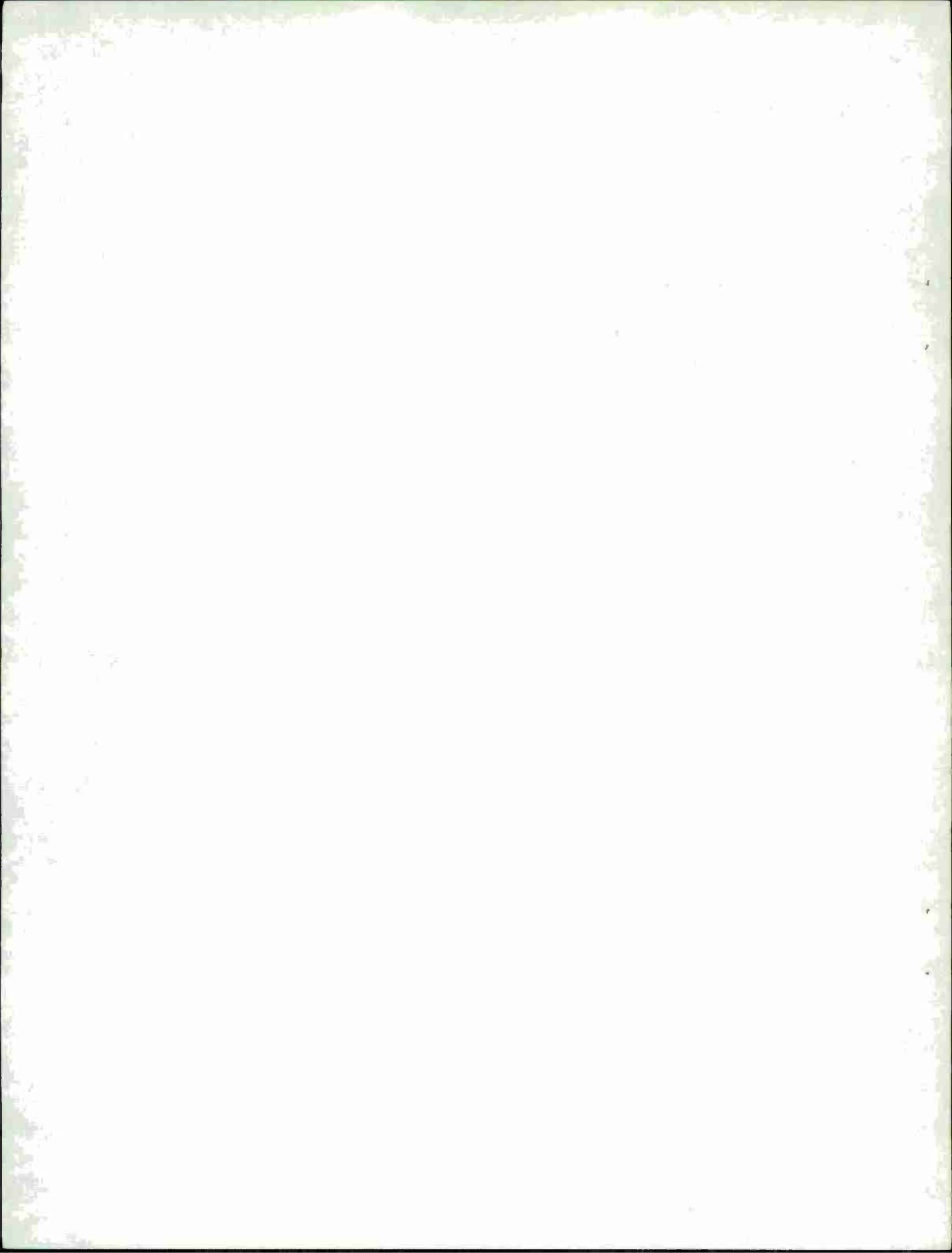
TABLES

(Table 1 may be found on page 10.)

TABLE 2

Beckman Readings on Three Dates

Target: 2024-T4 Aluminum

Wave-lengths (μm)	0.8	0.9	1.0	1.1	1.2	1.3	1.4	1.5
Dates								
24 Jun	.574	.597	.627	.655	.670	.688	.694	.712
25 Jun	.584	.607	.636	.660	.682	.697	.707	.721
1 Jul	.580	.602	.632	.655	.670	.683	.695	.708
Avg	.579	.602	.631	.656	.674	.689	.698	.713
Range	.010	.010	.009	.005	.012	.014	.013	.013
Std Dev	.006	.006	.005	.003	.007	.008	.007	.008

TABLE 3

EMR Readings on Three Dates

Target: 2024-T4 Aluminum

Wave-lengths (μm)	0.8	0.9	1.0	1.1	1.2	1.3	1.4	1.5
Dates								
24 Jun	.738	.737	.773	.840	.827	.843	.828	.830
25 Jun	.680	.693	.733	.742	.768	.786	.775	.775
28 Jun	.672	.679	.715	.730	.757	.775	.765	.755
Avg	.696	.703	.740	.770	.784	.801	.789	.786
Range	.066	.058	.058	.11	.07	.068	.063	.075
Std Dev	.039	.034	.034	.065	.041	.040	.037	.044
$\frac{\text{EMR-DK2A}}{\text{DK2A}}$	20.2	16.7	17.2	17.3	16.3	16.2	12.9	10.2

15.8% AVERAGE PERCENT DISAGREEMENT

$a = \sqrt{b^2 + f^2}$ SEMIMAJOR AXIS

$b = 5.50 \pm 0.01$ SEMIMINOR AXIS

$f = 2.00 \pm 0.01$ FOCAL DISTANCE
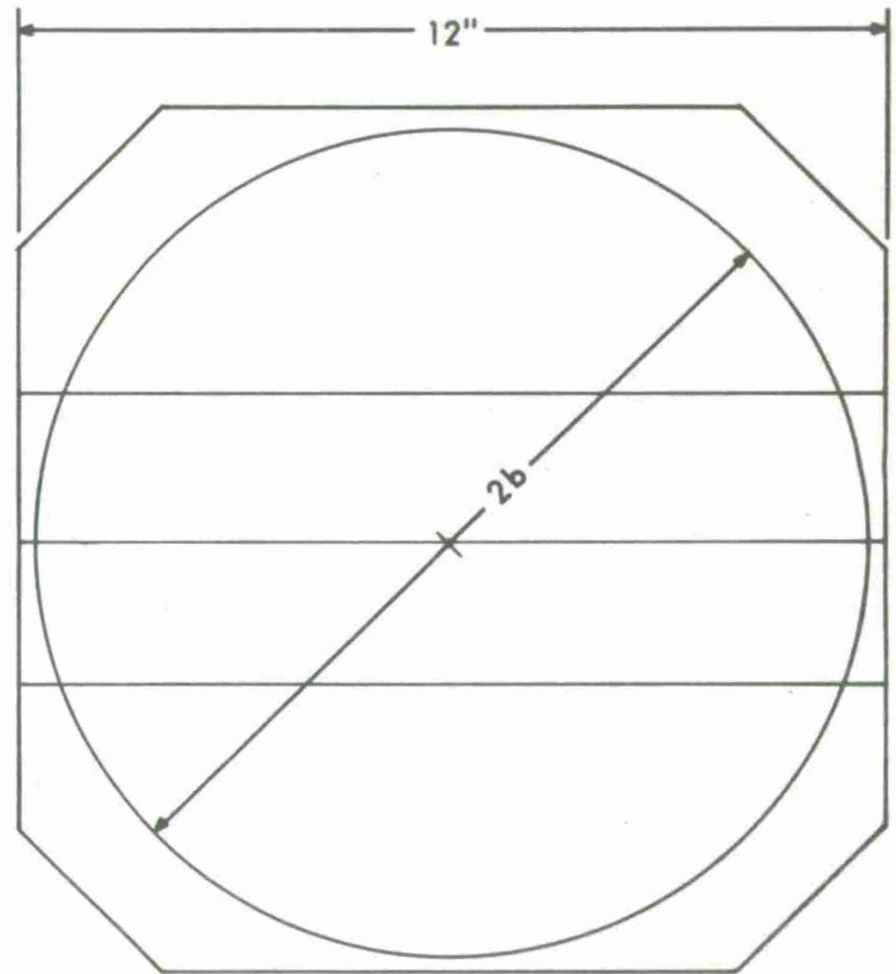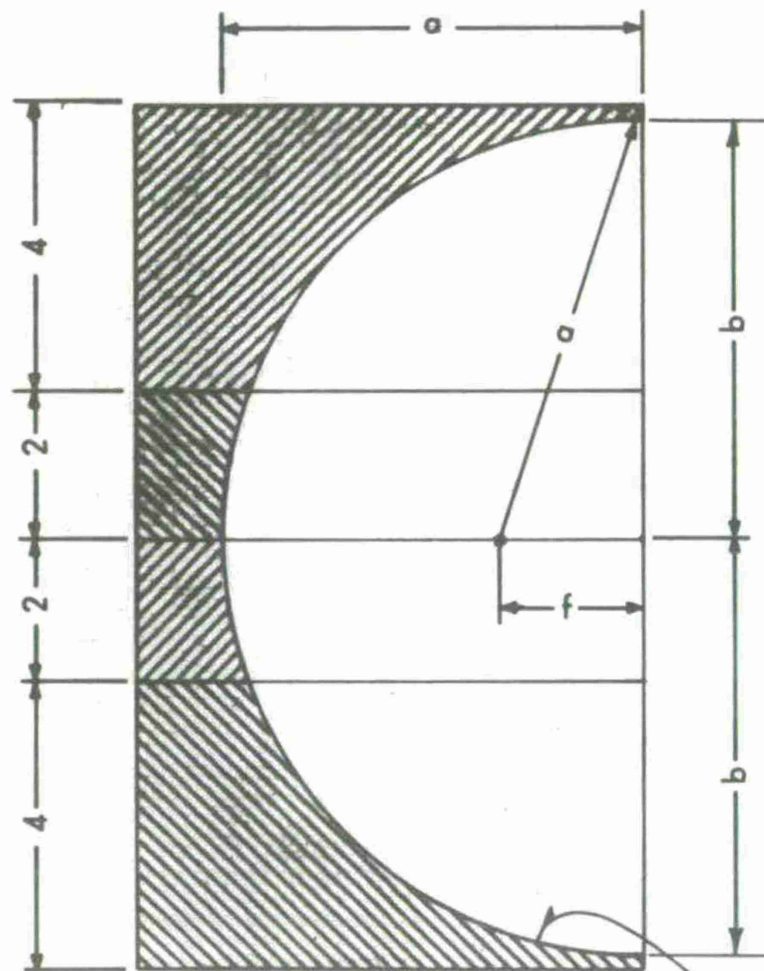
32 MICROFINISH
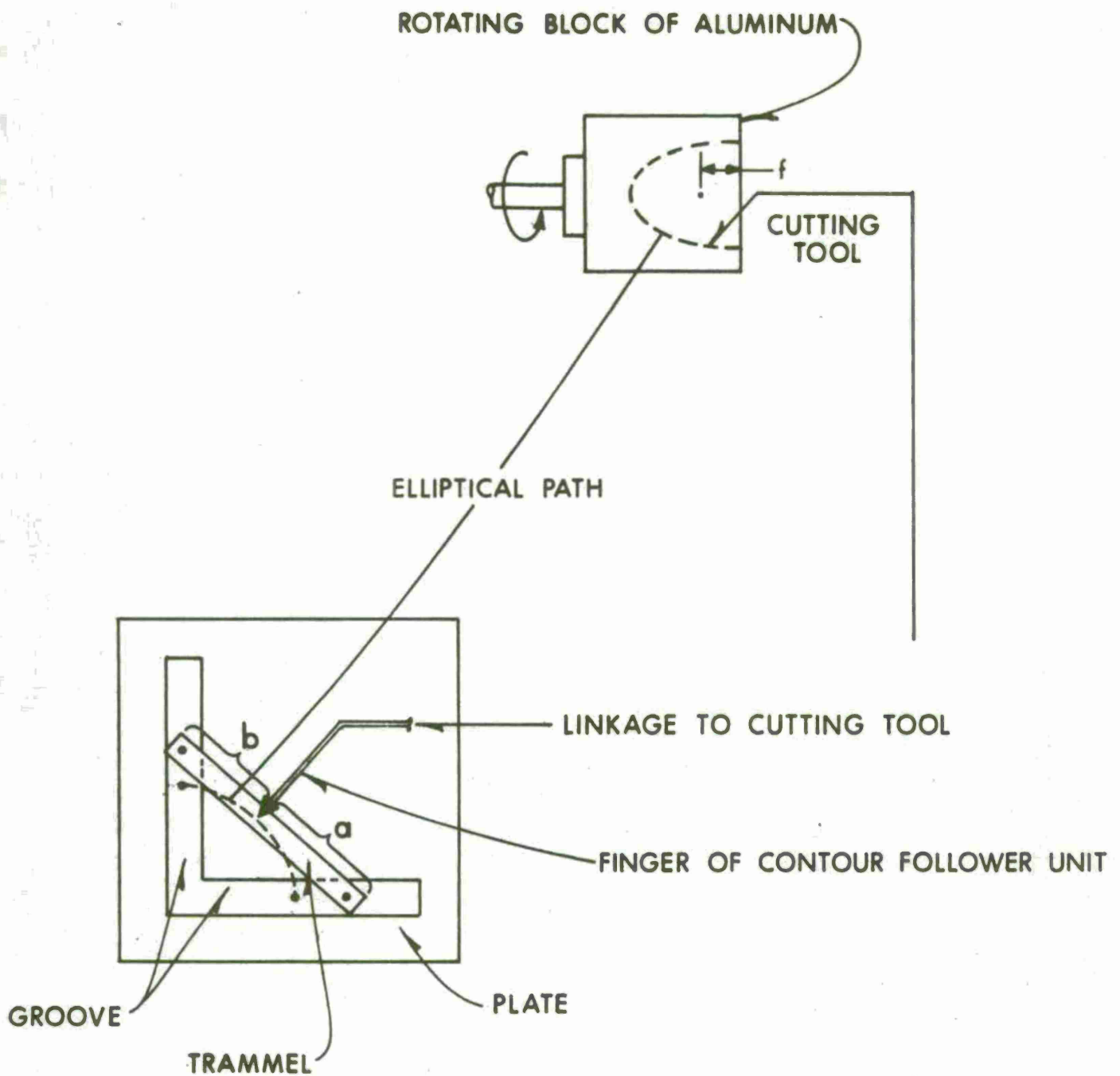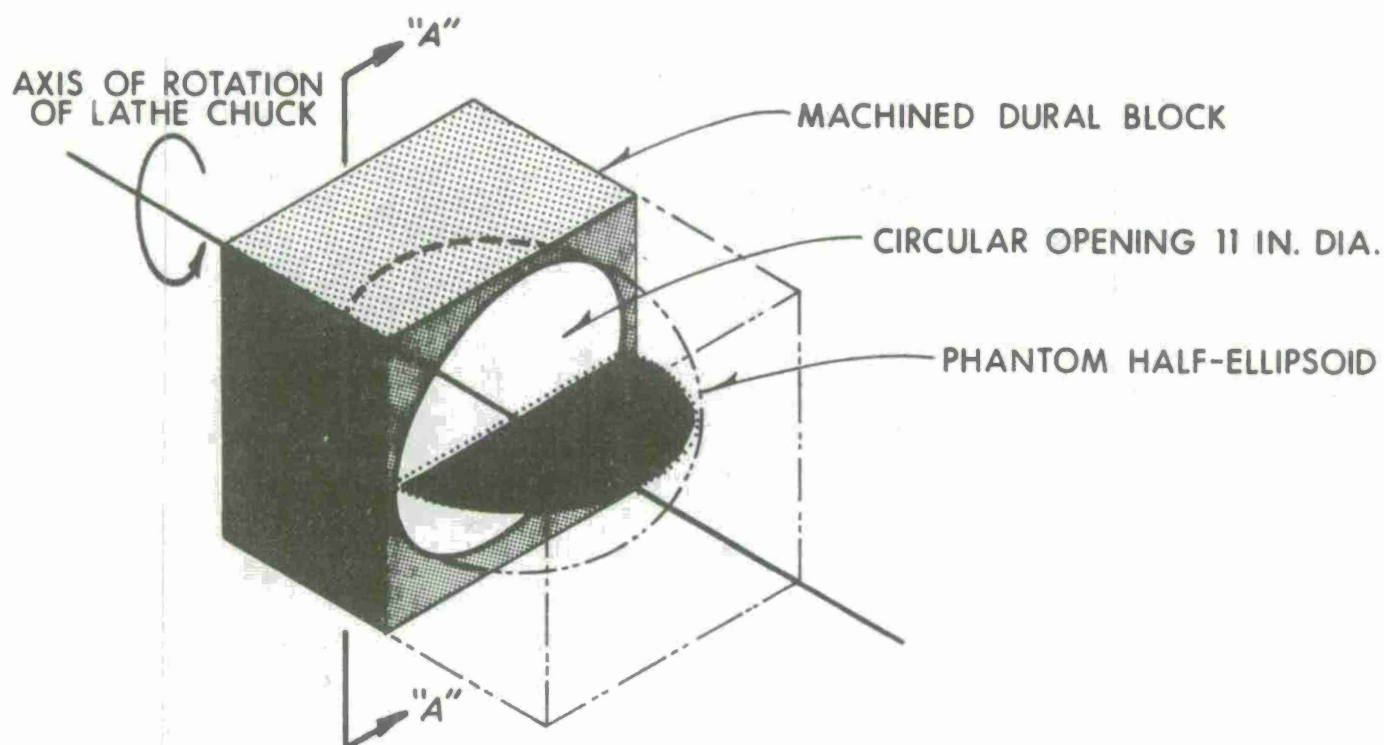
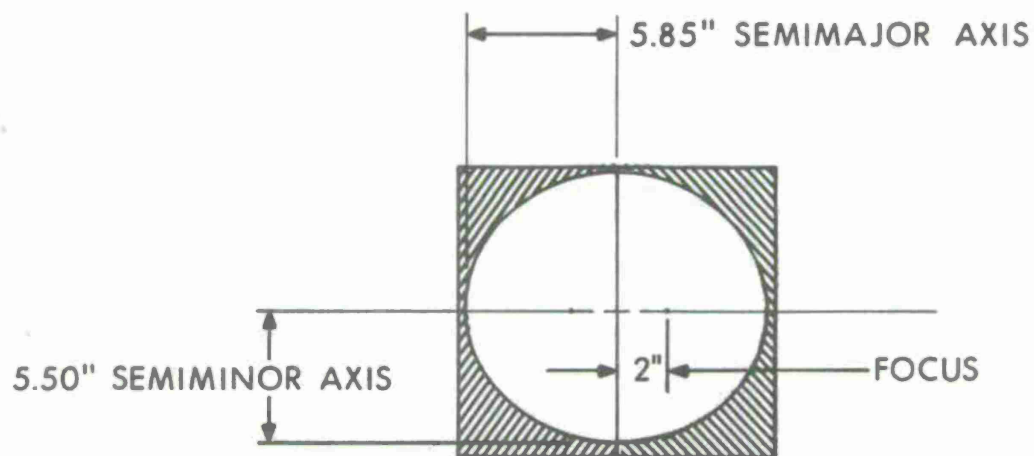Figure 1. Design of Half-Ellipsoidal Cavity

ROTATING BLOCK OF ALUMINUM

f

CUTTING
TOOL

ELLIPTICAL PATH

b

a

LINKAGE TO CUTTING TOOL

FINGER OF CONTOUR FOLLOWER UNIT

GROOVE

PLATE

TRAMMEL

$$\frac{a}{b} = \frac{\text{SEMIMAJOR AXIS}}{\text{SEMIMINOR AXIS}} = 1.06$$

Figure 2. Machining Half-Ellipsoidal Cavity

"A"

AXIS OF ROTATION
OF LATHE CHUCK

MACHINED DURAL BLOCK

CIRCULAR OPENING 11 IN. DIA.

PHANTOM HALF-ELLIPSOID

"A"

HALF-ELLIPSOID ON THE LATHE

5.85" SEMIMAJOR AXIS

5.50" SEMIMINOR AXIS

2"

FOCUS

REJOINED HALVES

NOTE: LEFT SIDE IS VIEW "A-A". RIGHT SIDE IS SYMMETRICAL
HALF CREATED BY CUT IN PLANE "A-A".

Figure 3.   Sectioning of Half-Ellipsoid

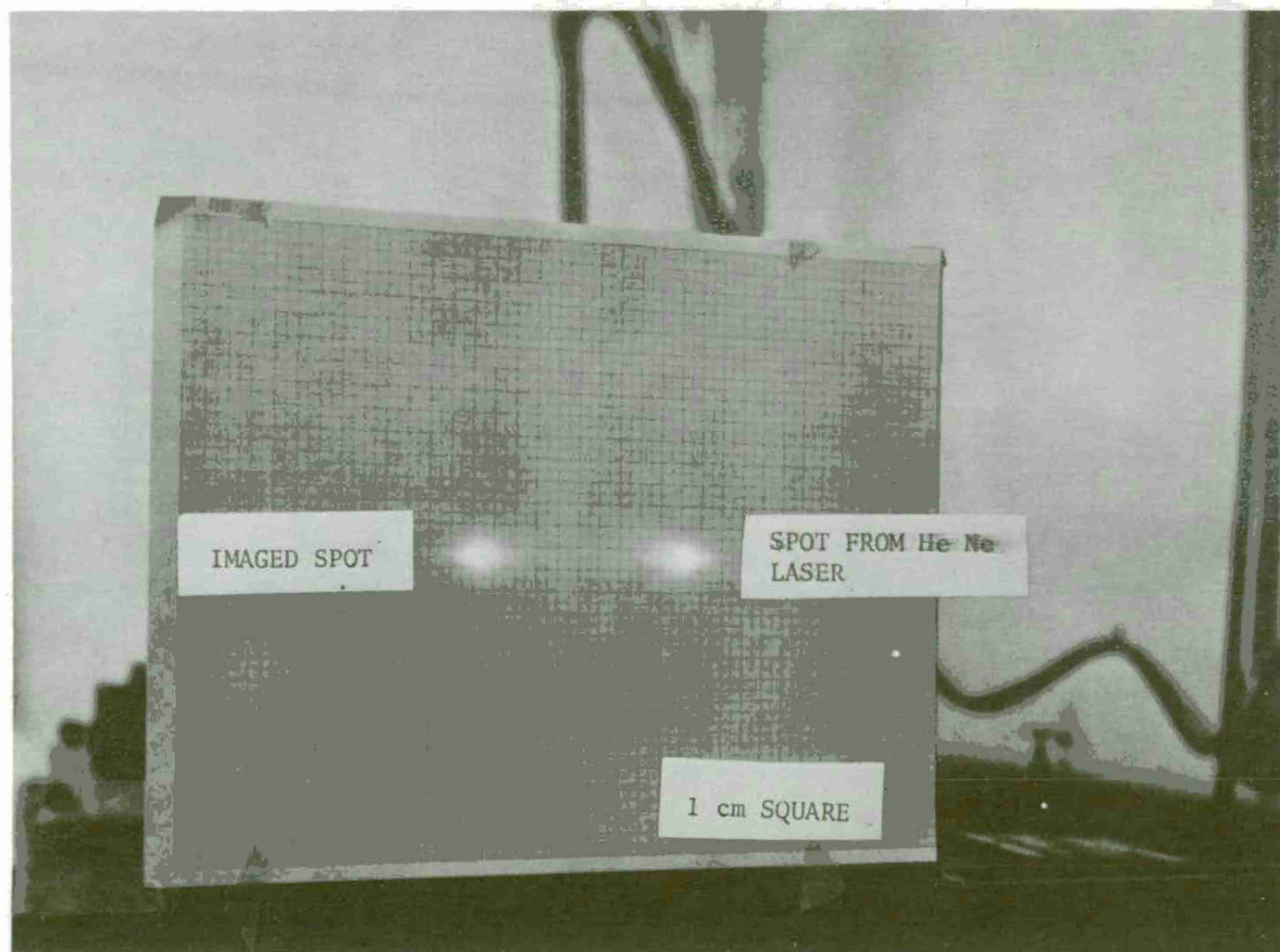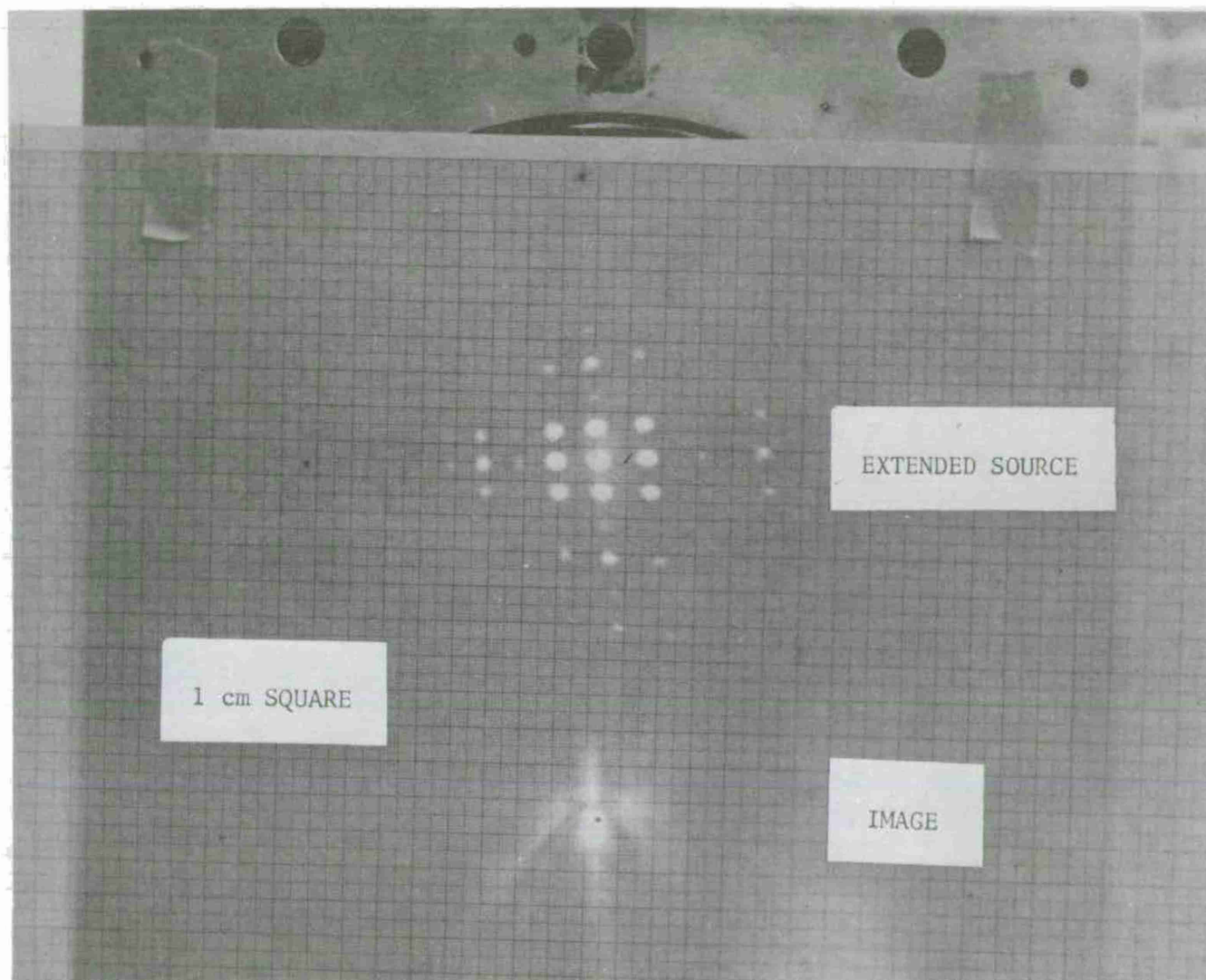Figure 4. Imaging of a Spot Source

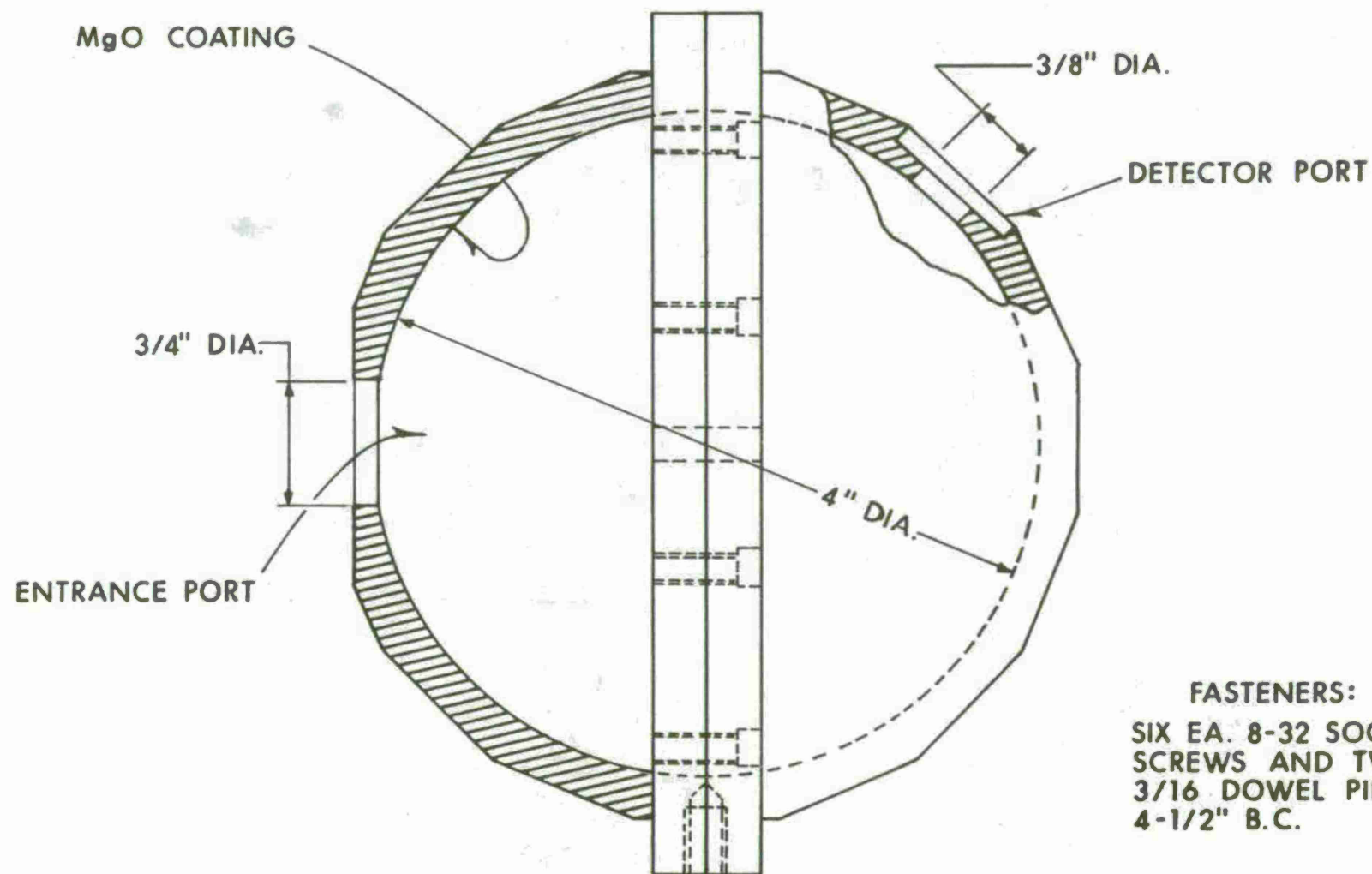Figure 5. Imaging of an Extended Source

MgO COATING

3/8" DIA.

DETECTOR PORT

3/4" DIA.

4" DIA.

ENTRANCE PORT

FASTENERS:

SIX EA. 8-32 SOC. HD.
SCREWS AND TWO EA.
3/16 DOWEL PINS ON
4-1/2" B.C.
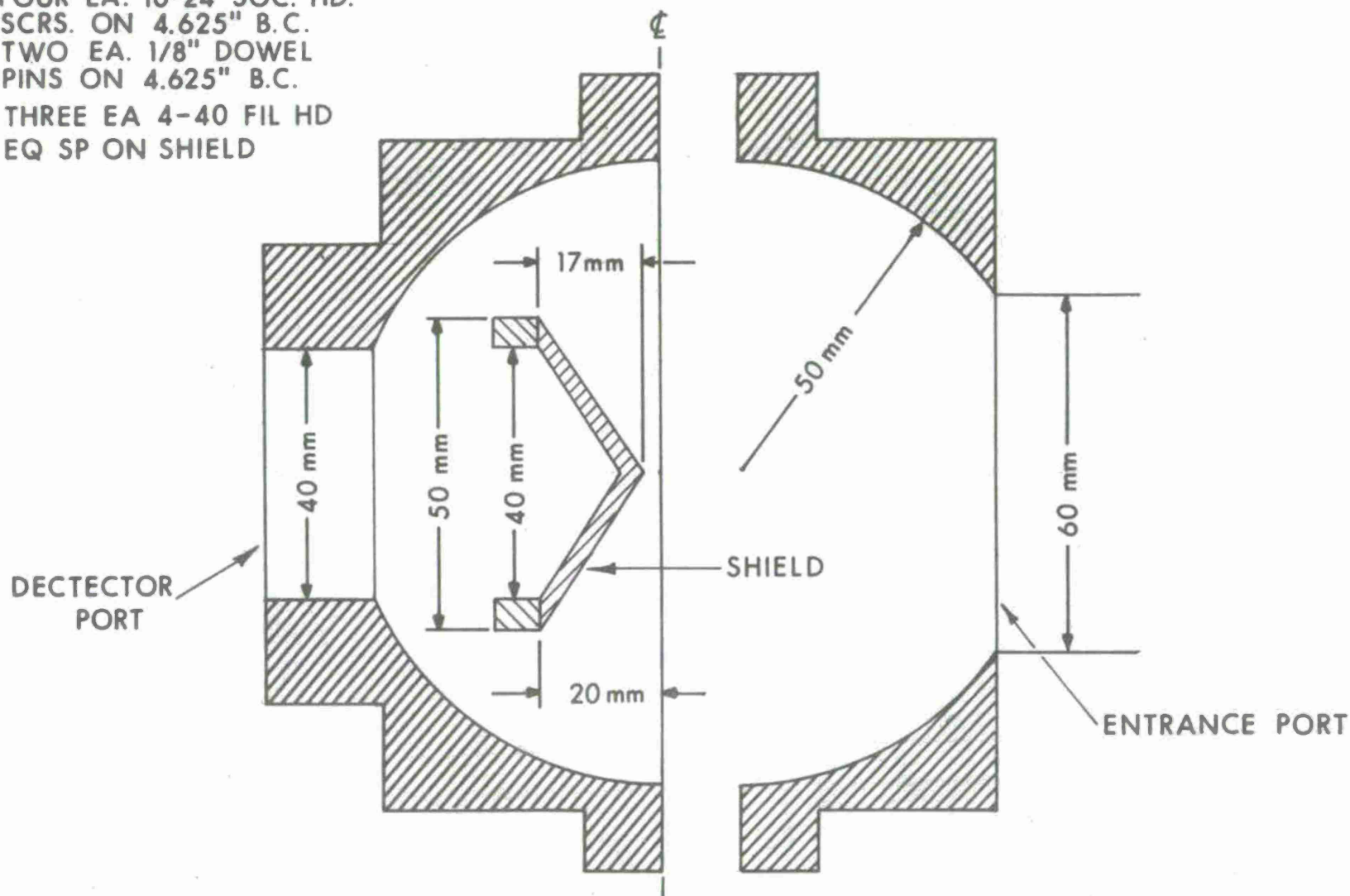
Figure 6. Unshielded Averaging Sphere

Figure 7 Larche-Schulze Averaging Sphere
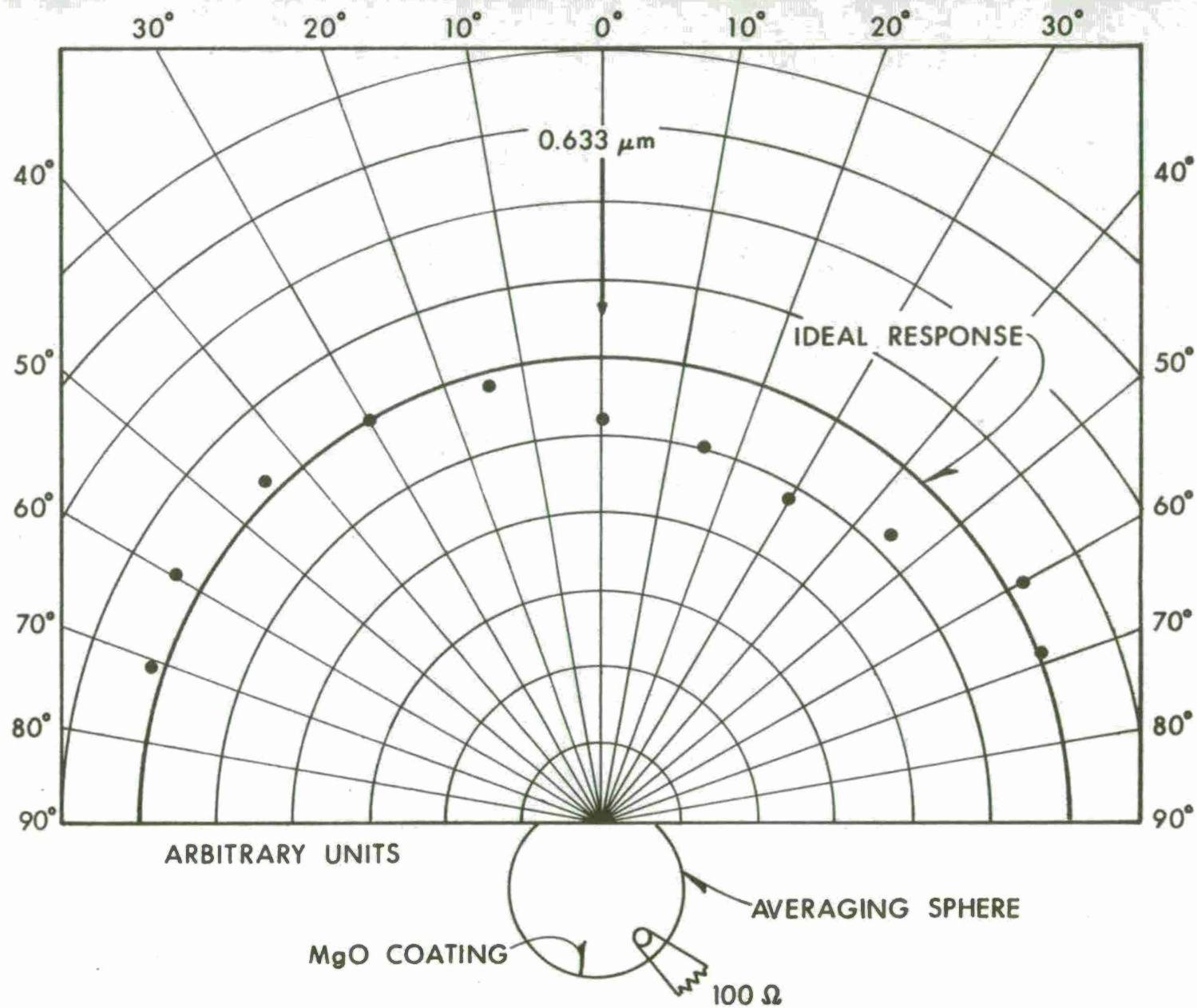
Figure 8. Response of Unshielded Sphere to Narrow Beam Illumination

44
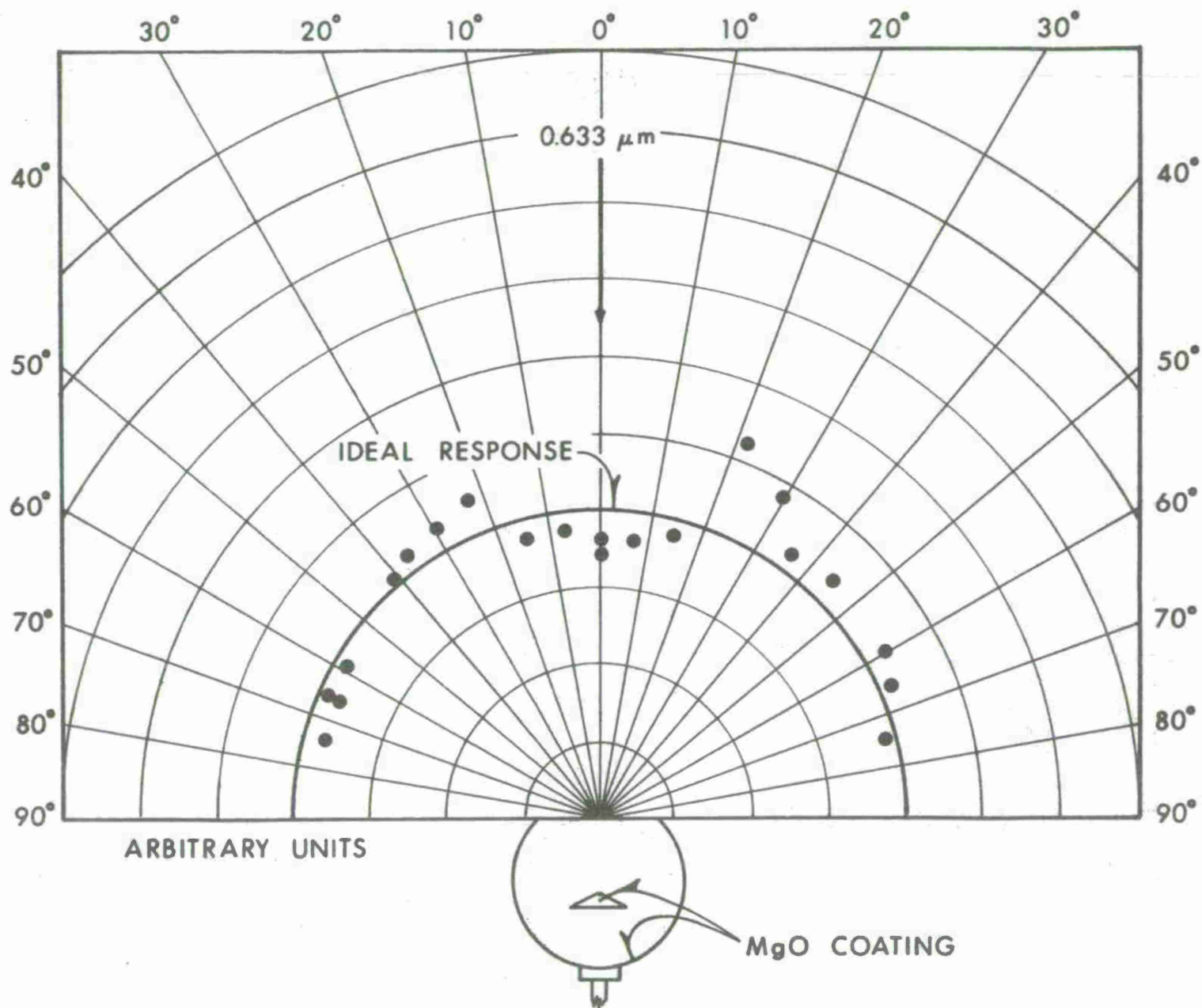
Figure 9. Response of Larche-Schulze Sphere to Narrow Beam Illumination
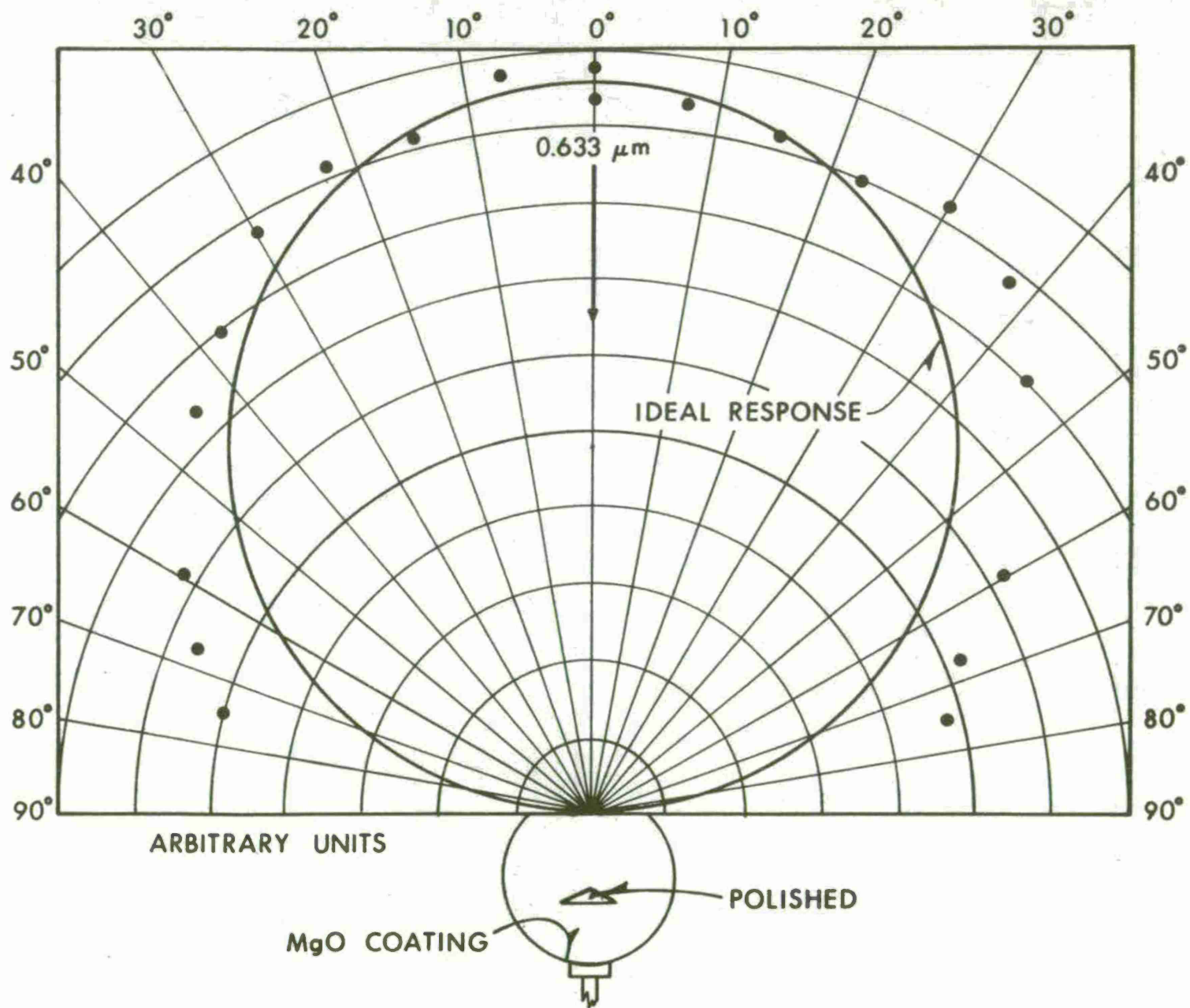
Figure 10. Response of Larche-Schulze Sphere to Full-Beam Illumination

46
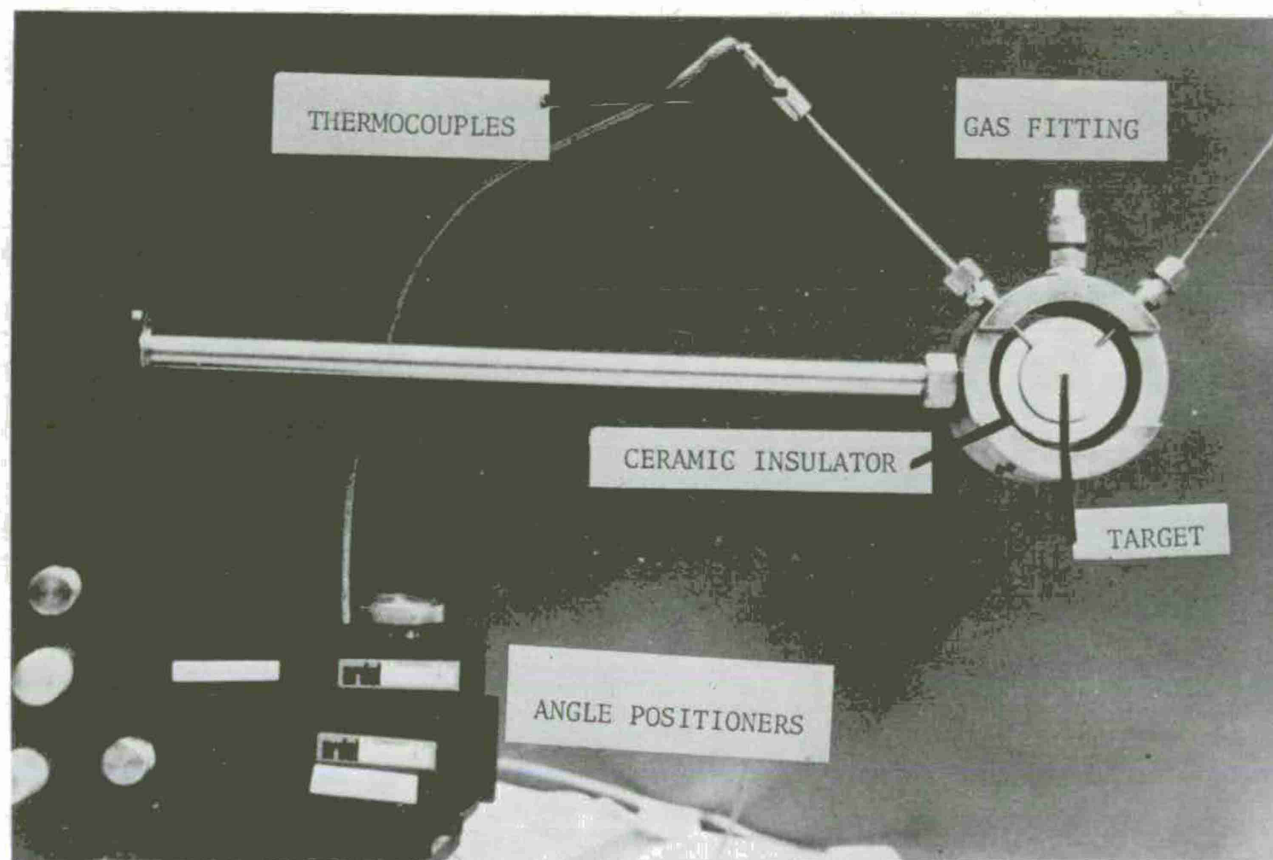
Figure 11. Target Mounted
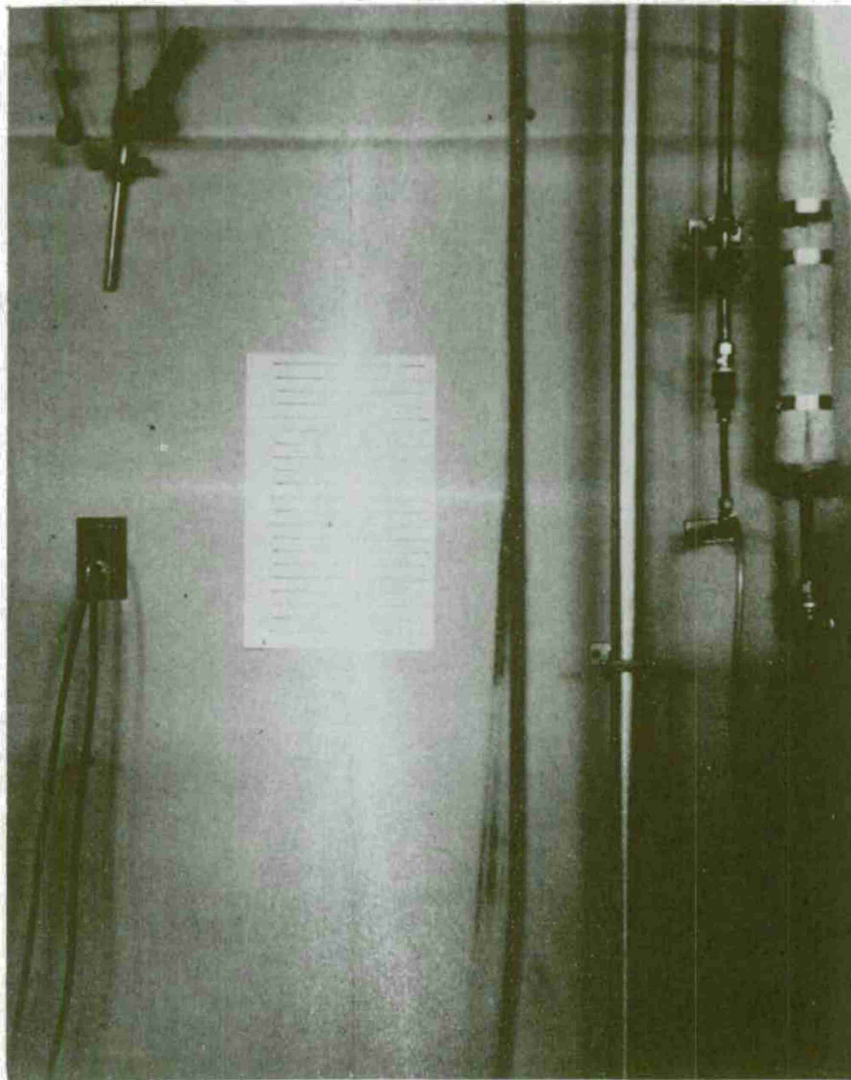
Figure 12.   Reflection Pattern from Scratched Target

Figure 13. Unidirectional Lay of Surface

Figure 14. Reflectance Apparatus

OSCILLOSCOPE

LOCK IN AMPLIFIER

ELLIPSOIDAL MIRROR

LAMP

DETECTOR

UNSHIELDED
AVERAGING
SPHERE

DVM

XY RECORDER

Figure 15. Reflectance Apparatus

Figure 16. Sample Measured on EMR
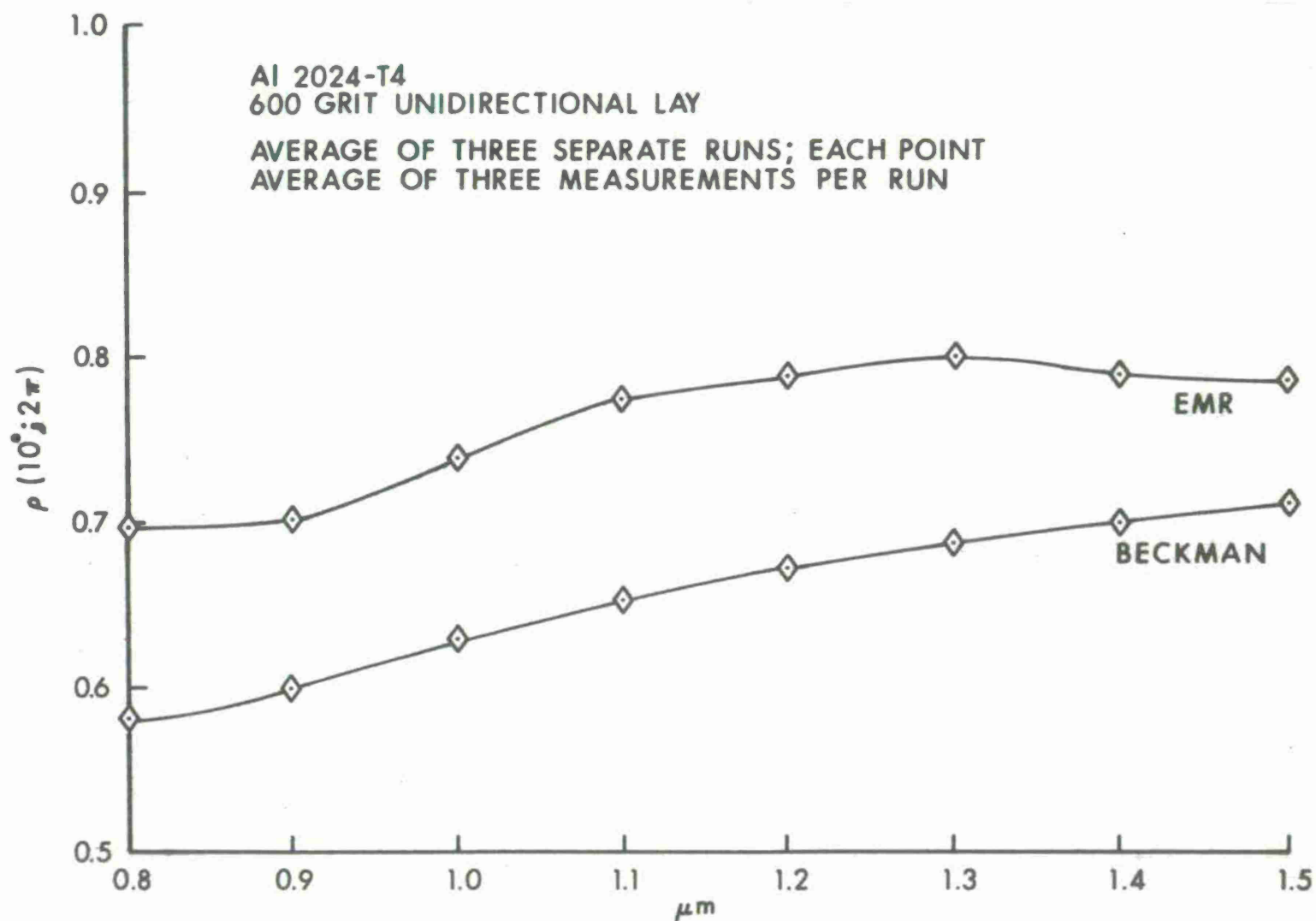
Figure 17. Comparison of EMR and Beckman

DISTRIBUTION LIST

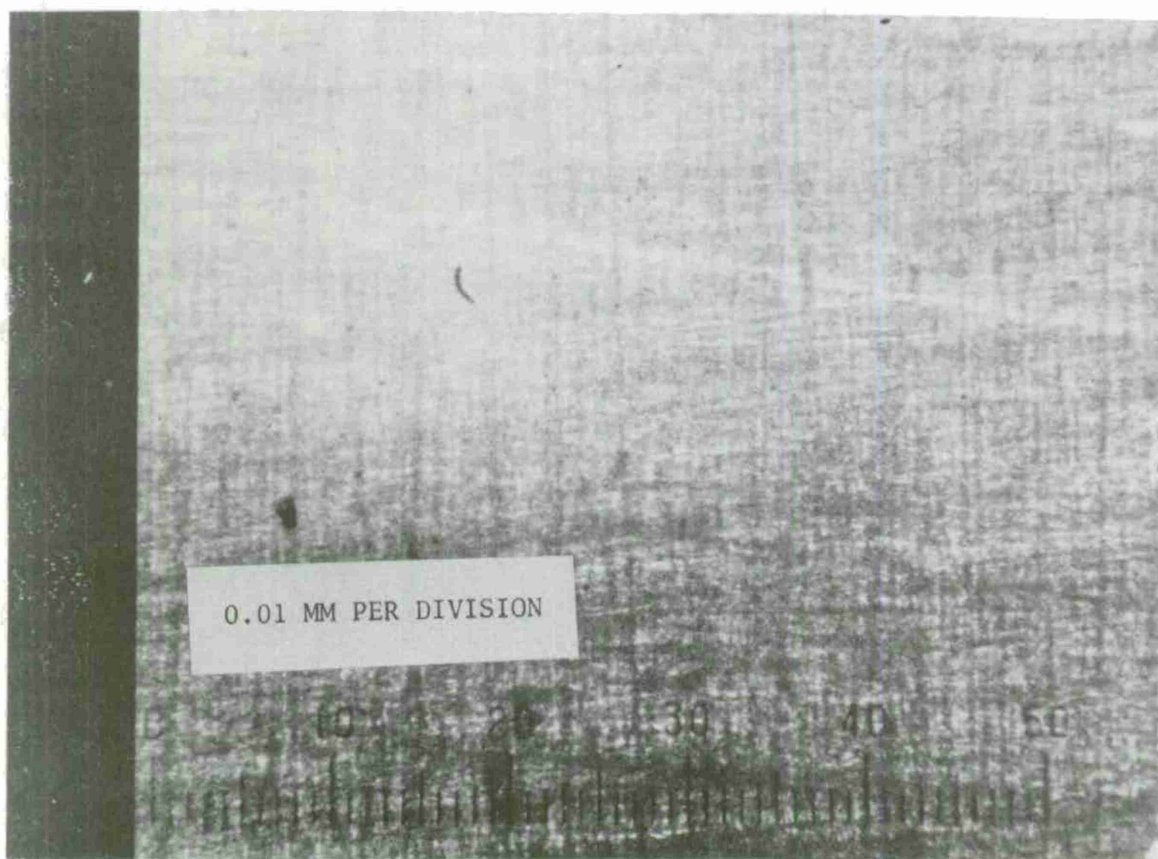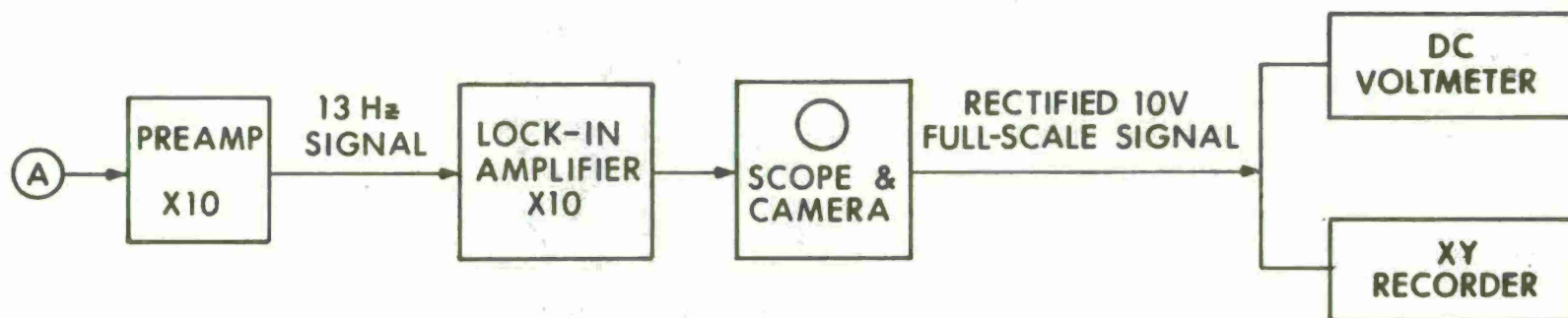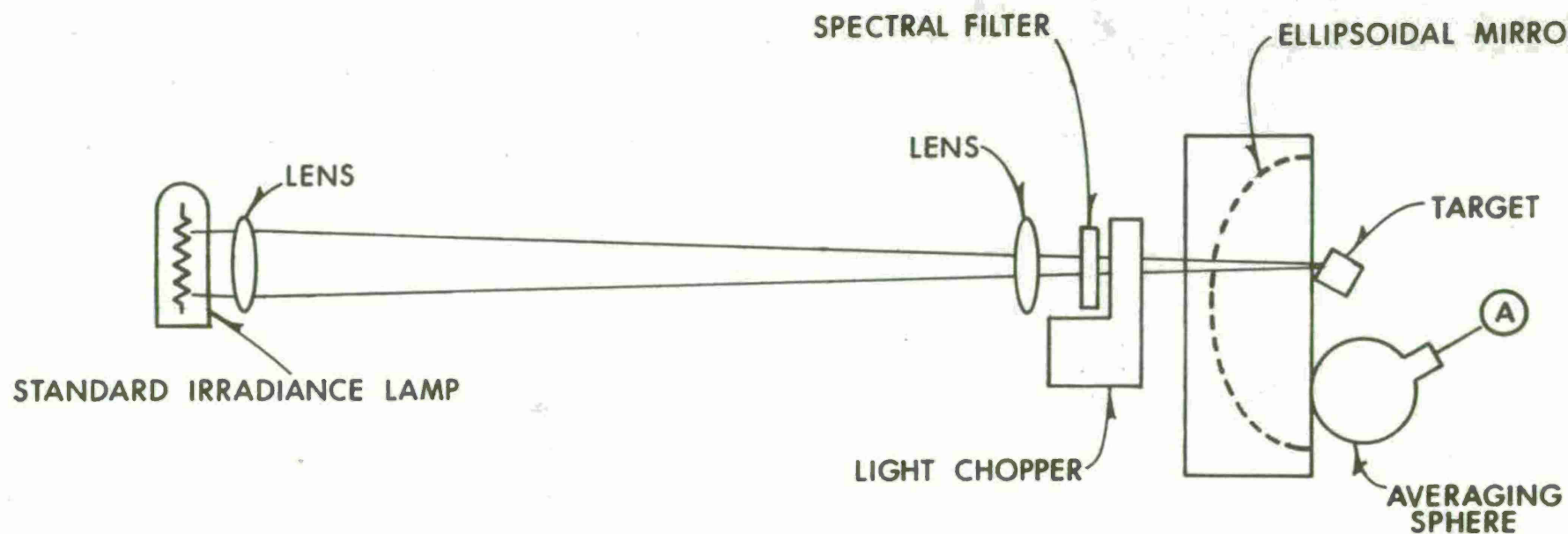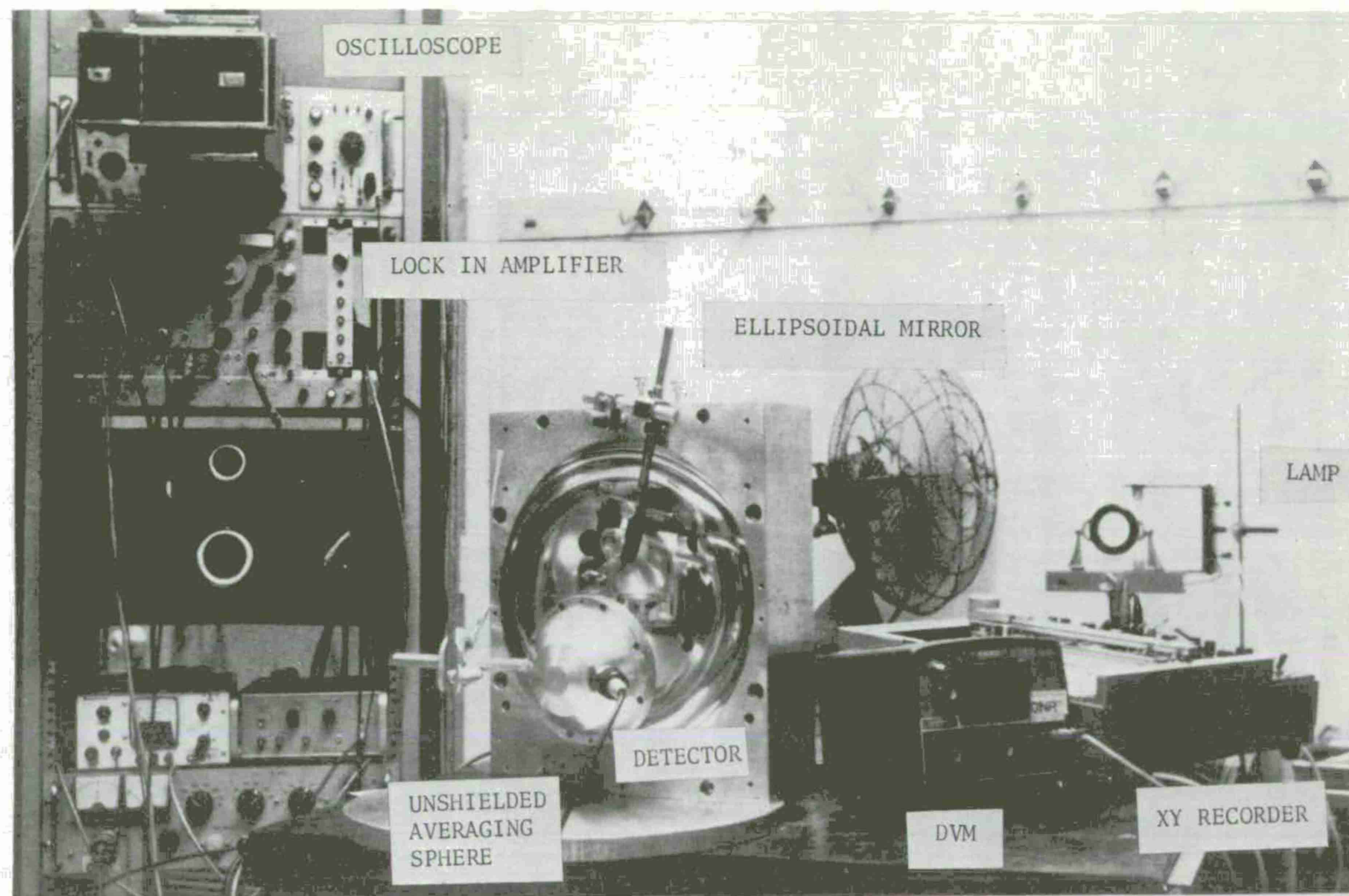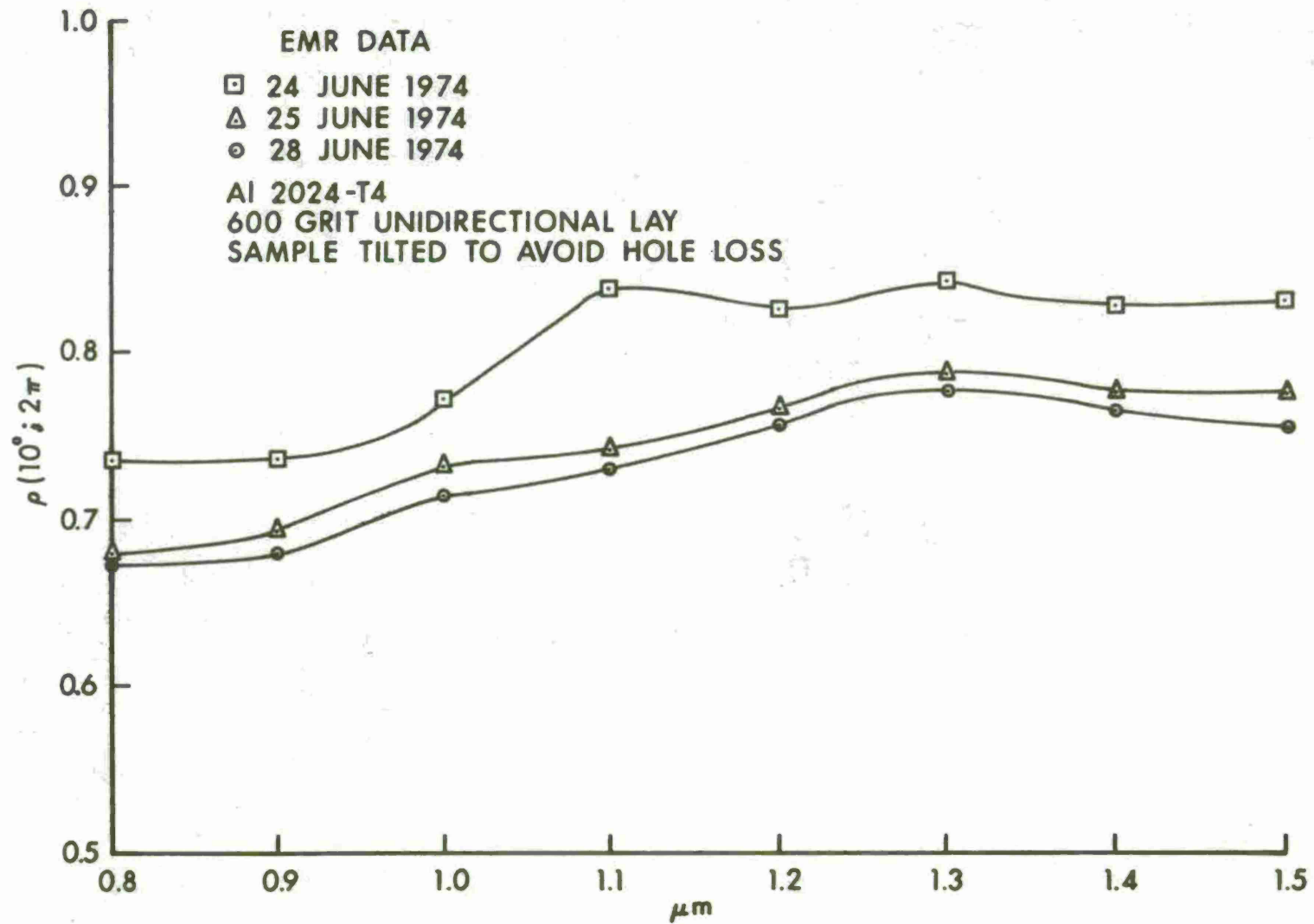| No. of Copies	Organization	No. of Copies	Organization
12	Commander Defense Documentation Center ATTN: DDC-TCA Cameron Station Alexandria, VA 22314	1	Commander US Army Materiel Command ATTN: AMCPM-AI, Mr. Cory 5001 Eisenhower Avenue Alexandria, VA 22333
1	Director Institute for Defense Analyses ATTN: Tech Lib 400 Army Navy Drive Arlington, VA 22202	1	Commander US Army Aviation Systems Command ATTN: AMSAV-E 12th and Spruce Streets St. Louis, MO 63166
1	Chairman Defense Science Board Washington, DC 20301	1	Director US Army Air Mobility Research and Development Laboratory Ames Research Center Moffett Field, CA 94035
1	Director Defense Intelligence Agency ATTN: Mr. Seymour Berler DIAST-2B Washington, DC 20301	4	Commander US Army Electronics Command ATTN: AMSEL-RD, Dr. Wiseman AMSEL-CT/L Dr. R. G. Buser Mr. B. Louis AMSEL-TL/I-J Dr. H. Jacobs Fort Monmouth, NJ 07703
1	Commander US Army Materiel Command ATTN: AMCDMA-ST 5001 Eisenhower Avenue Alexandria, VA 22333		
1	Commander US Army Materiel Command ATTN: AMCRD-T 5001 Eisenhower Avenue Alexandria, VA 22333	1	Commander US Army Electronics Command ATTN: AMSEL-PP-E-P/IED 225 South 18th Street Philadelphia, PA 19103
1	Commander US Army Materiel Command ATTN: AMCRD-R 5001 Eisenhower Avenue Alexandria, VA 22333	1	Commander US Army Electronics Command and Development Activity ATTN: Mr. R. Nelson White Sands Missile Range New Mexico 88002
1	Commander US Army Materiel Command ATTN: AMCRD-W, Mr. Darr 5001 Eisenhower Avenue Alexandria, VA 22333	1	Director Night Vision Laboratory ATTN: AMSEL-NV-OR, Mr. Gibson Fort Belvoir, VA 22060

DISTRIBUTION LIST

No. of Copies	Organization	No. of Copies	Organization

3	Commander
	US Army Missile Command
	ATTN: AMSMI-R
	        AMSMI-RR
	              Dr. J.P.Hallowes, Jr.
	              Mr. W.B.Jennings, Jr.
	Redstone Arsenal, AL 35809
		1	Commander
			US Army Armament Command
			Rock Island, IL 61202

3	Commander
	US Army Missile Command
	ATTN: AMSMI-RR, J. Hammond
	        AMSSM-RRP
	              Dr. T. A. Barr, Jr.
	              Mr. Andrew Jenkins
	Redstone Arsenal, AL 35809
		3	Commander
			US Army Frankford Arsenal
			ATTN: SARFA-L5000, Dr. K. Green
			        SARFA-A1000, Dr. S. Ross
			        SARFA-L9000, J. Helfrich
			Philadelphia, PA 19137

3	Commander
	US Army Missile Command
	ATTN: AMSMI-RRR
	              Dr. T. G. Miller
	        AMSMI-RRS
	              Dr. W. McKnight
	              Dr. R. W. Conrad
	Redstone Arsenal, AL 35809
		1	Commander
			US Army Picatinny Arsenal
			ATTN: SARPA-VL, Mr. Kisatsky
			Dover, NJ 07801

1	Commander US Army Tank Automotive Command ATTN: AMSTA-RHFL Warren, MI 48090	1	Commander US Army Electronic Proving Ground ATTN: STEEP-OC Fort Huachuca, AZ 85613

2	Commander
	US Army Mobility Equipment
	   Research & Development Center
	ATTN: Tech Docu Cen, Bldg. 315
	        AMSME-RZT
	Fort Belvoir, VA 22060
		1	Commander
			Deseret Test Center
			Dugway Proving Ground
			Dugway, UT 84022

4	Commander
	US Army Mobility Equipment
	   Research & Development Center
	ATTN: SMEFB-MN, Dr. R. Lasken
	              Dr. J. Fox
	        SMEFB-MW, Dr. J. Bond
	              Mr. D. Barr
	Fort Belvoir, VA 22060
		1	Commander
			US Army Jefferson Proving Ground
			ATTN: STEJP-TD-D
			Madison, IN 47251

		1	Commander US Army Yuma Proving Ground ATTN: STEYP-AD, Tech Lib Yuma, AZ 85364
		1	Commander US Army White Sands Missile Range ATTN: STEWS-IB, Mr. Miller White Sands, NM 88002

DISTRIBUTION LIST

No. of Copies	Organization	No. of Copies	Organization
2	Commander US Army Rock Island Arsenal ATTN: SARRI, Dr. E. Haug 　　　　Mr. Reinsmith Rock Island, IL 61202	1	President US Army Armor and Engineer 　Board ATTN: STEBB-CV Fort Knox, KY 40121
2	Commander US Army Harry Diamond Labs ATTN: AMXDO-TI 　　　　AMXDO-RCB/320 　　　　Mr. Gibson 2800 Powder Mill Road Adelphi, MD 20783	1	President US Army Artillery Board Fort Sill, OK 73504
		1	President US Army Artillery Board Fort Sill, OK 73504
4	Commander US Army Materials and 　Mechanics Research Center ATTN: AMXMR-ATL, Tech Lib 　　　　AMXMR-EC 　　　　Dr. Paul Sagalyn 　　　　Mr. L.D. Jennings 　　　　Dr. R. Fitzpatrick Watertown, MA 02172	1	President US Army Aviation Test Board ATTN: STEBG-TP-V Fort Rucker, AL 36362
		1	President US Army Infantry Board ATTN: STEBC-SW Fort Benning, GA 31905
2	Commander US Army Natick Laboratories ATTN: AMXRE-PRD, Mr. J. Roach 　　　　STSNL-CTR, Dr. E. Healy Natick, MA 01762	2	HQDA (DAMA-ARP, Dr. Watson; 　DAMA-ARZ-A, BG Daniel) Washington, DC 20310
1	Commander US Army Foreign Science and 　Technology Center ATTN: AMXST-BS Munitions Building Washington, DC 20315	1	Commander US Army Medical Research and 　Development Command ATTN: COL R. W. Neidlinger Washington, DC 20315
		1	Commander US Army Medical Research Lab Fort Knox, KY 40120
1	Director US Army TRADOC Systems Analysis 　Activity ATTN: ATAA-SA White Sands Missile Range New Mexico 88002	1	Commander US Army Topographic Command ATTN: Lib Washington, DC 20315

DISTRIBUTION LIST

No. of
Copies   Organization

1 Commander
  US Army Cold Regions Research
    and Engineering Laboratories
  ATTN: Mr. B. Hansen
  Hanover, NH 03775

1 Commander
  US Army Research Office
  P. O. Box 12211
  Research Triangle Park, NC
  27709

2 Chief of Naval Operations
  Department of the Navy
  ATTN: OP-07T-1, B. Rosenberg
        OP-723, CAPT Wilson
  Washington, DC 20350

1 Chief of Naval Material
  Department of the Navy
  ATTN: RADM A.S. Goodfellow
  Washington, DC 20360

2 Chief of Naval Research
  Department of the Navy
  ATTN: Code 421, F. Isakson
  Washington, DC 20360

1 Office of Naval Research
  ATTN: Dr. Fred Quelle
  495 Summer Street
  Boston, MA 02210

3 Commander
  US Naval Air Systems Command
  ATTN: AIR-604
  Washington, DC 20360

2 Commander
  US Naval Ordnance Systems
    Command
  ATTN: ORD-9132
        ORD-0832, J.C. Zelebor
  Washington, DC 20360

No. of
Copies   Organization

1 Commander
  US Army Missile Center
  ATTN: Code 5352, G. Gibbs
  Point Mugu, CA 93042

1 Commander
  US Naval Surface Weapons Center
  Dahlgren, VA 22448

2 Commander
  US Naval Surface Weapons Center
  ATTN: Code 310
        Dr. L. H. Schindel
        Dr. E. W. Eagleson
  Silver Spring, MD 20910

1 Commander
  US Naval Weapons Center
  China Lake, CA 93555

3 Director
  US Naval Research Laboratory
  ATTN: Code 6330
        Dr. A. I. Schindler
        Dr. T. Schriempf
        Mr. R. Stegman
  Washington, DC 20390

1 Commander
  US Naval Postgraduate School
  ATTN: John R. Neighbours
        Professor of Physics
  Monterey, CA 93940

2 HQ USAF (AFRSTE; AFRDDE, COL
    Orlando Wall)
  Washington, DC 20330

1 AFSC
  Andrews AFB
  Washington, DC 20331

1 AFATL (DLDL, MAJ J.E. Morgan)
  Eglin AFB, FL 32542

DISTRIBUTION LIST

No. of Copies	Organization	No. of Copies	Organization
1	AFATL (DLRB) Eglin AFB, FL 32542	1	General Research Corporation Operations Analysis Division Westgate Research Park McLean, VA 22101
1	RADC (Mr. Frank J. Rehm) Griffiss AFB, NY 13440		
2	AFWL (SUL; LTC J.Kurzenberger) Kirtland AFB, NM 87117	1	Heliodyne Corporation ATTN: Dr. R. Grandey 11689 Sorrento Valley Road San Diego, CA 92121
1	AFAL (AVTL, K. Hutchinson) Wright-Patterson AFB, OH 45433	2	Honeywell Corporate Research Center Honeywell, Incorporated ATTN: Mr. Jack Ready, C1300 Mr. E. Bernal G. 10701 Lyndale Avenue, South Bloomington, MN 55420
1	FTD/PDTN-4 Wright-Patterson AFB, OH 45433		
1	Director P. O. Box 1925 ATTN: Julian C. Nall Washington, DC 20505		
		1	Hughes Research Laboratories ATTN: Dr. D. Foster 3011 Malibu Canyon Road Malibu, CA 90265
1	Advisory Group on Electron Devices ATTN: Secy, Sp Gp on Opt Masers 201 Varick Street New York, NY 10014	1	Lincoln Laboratory ATTN: Dr. S. Edelberg P. O. Box 73 Lexington, MA 02173
1	Aerospace Corporation P. O. Box 95085 Los Angeles, CA 90045	1	Lockheed Palo Alto Research Lab Lockheed Missiles and Space Company, Incorporated A Subsidiary of Lockheed Aircraft Corporation ATTN: D. M. Aspinwall 3251 Hanover Street Palo Alto, CA 94304
2	AVCO-Everett Research Lab ATTN: Mr. R. E. Janney Dr. B. Feinberg 2385 Revere Beach Parkway Everett, MA 02149		
1	Boeing Company ATTN: Dr. Russell V. Hanks Seattle, WA 98124	1	McDonnell Douglas Astronautics Company 5301 Bolsa Avenue Huntington Beach, CA 92647
1	General Research Corporation ATTN: Dr. Richard Holbrook P. O. Box 3587 Santa Barbara, CA 93015	1	McDonnell Douglas Aircraft Company P. O. Box 516 St. Louis, MO 63166

DISTRIBUTION LIST

No. of Copies	Organization
1	Pratt and Whitney Aircraft Division Florida Research and Development Center ATTN: E. H. Pinsley West Palm Beach, FL 33402
1	Rand Corporation ATTN: Mr. Paul Tamarkin 1700 Main Street Santa Monica, CA 90406
2	United Aircraft Research Corp ATTN: Mr. G. H. McLafferty Mr. B. B. Silverman 400 Main Street East Hartford, CT 06108
2	The Johns Hopkins University Applied Physics Laboratory ATTN: Dr. Albert M. Stone Dr. Lou Weckesser Johns Hopkins Road Laurel, MD 20783

No. of Copies	Organization
1	Riverside Research Institute ATTN: Dr. L. H. O'Neill 80 West End Avenue New York, NY 10023

Aberdeen Proving Ground

Marine Corps Ln Ofc
Dir, USAMSAA
Dir, USAMTD
 ATTN: STEAP-MT
Cmdt, USAOC&S
 ATTN: ATSL-D
Cmdr, USEA
 ATTN: SAREA-DE-W, A. Flatau